npj computational materials

www.nature.com/npjcompumats

REVIEW ARTICLE OPEN

Check for updates

Understanding and design of metallic alloys guided by phase-field simulations

Yuhong Zhao [1,2,3]✉

Phase-field method (PFM) has become a mainstream computational method for predicting the evolution of nano and mesoscopic microstructures and properties during materials processes. The paper briefly reviews latest progresses in applying PFM to understanding the thermodynamic driving forces and mechanisms underlying microstructure evolution in metallic materials and related processes, including casting, aging, deformation, additive manufacturing, and defects, etc. Focus on designing alloys by integrating PFM with constitutive relations and machine learning. Several examples are presented to demonstrate the potential of integrated PFM in discovering new multi-scale phenomena and high-performance alloys. The article ends with prospects for promising research directions.

npj Computational Materials (2023)9:94 ; https://doi.org/10.1038/s41524-023-01038-z

INTRODUCTION

Understanding the relationship among "composition-processing-microstructure-properties" is the central theme of materials science and engineering[1]. Historically, the design of new materials has predominantly relied on the "trial-error" method to adjust and analyze alloy composition and process parameters, which requires a long cycle and high costs[2–5]. Multiscale modeling and computing methods, briding atomic scale structures to macro properties, are playing an increasing role in understanding and interpreting experimental observations and reducing experimental costs.

Mean field approaches are popular for approximating large complex stochastic models that contain large number of interacting bodies. By averaging the multi-body interaction into single-body interaction, the mean-field approximation theory (MFT) has become basis of some computational models, such as Weiss molecular field theory (WMF), Bragg-Williams Mean field theory (BW-MFT), Landau theory, density functional theory (DFT) and phase-field methods (PFM), etc. In addition to mean field approaches, there are many other microstructure simulation models, such as Molecular dynamics method (MD), Cellular Automata method (CA), Monte Carlo method (MC), Level Set Method (LSM), Front Tracking Method (FTM), Envelope Method (EM), Mean radius approach (MRA), and Kampmann-Wagner numerical method (KWN), etc. Commonly used microstructure simulation approaches and some cases are presented in Fig. 1. PFM is derived based on MFT and can uniquely provide critical links at both nanoscale and mesoscale, including morphology, size, spatial arrangement, transition path, defects, stress and strain distribution of various phases under complex internal or/and external effects.

The term "phase-field (PF)" was originally proposed to model mesoscale solidified dendrites[6], with phase ∅ and concentration *C*as non-conserved and conserved field variables respectively, which is the prototype of the continuous phase-field model (CPFM). In 1991, Chen adopted the atom occupation probability *P* as the conserved field variable to establish a microscopic diffuse phase-field model (MPFM) for phase separation of binary alloys, including atomic clustering and order-disorder transformation[7]. In 2002, Elder used the average atom density ρ as a conserved field variable to develop the phase-field-crystal (PFC) model for wider applications, even graphene materials[8]. PFM does not need to presuppose initial microstructure configuration and track the phase or grain boundary, allowing multiple fields to be easily added together, i.e., chemical, thermal, mechanical, magnetic, electrical, and other fields, to facilitate the opening or closing the effect of one or more internal or external fields to describe the microstructure and performance evolution in materials process. Therefore, the versatility and flexibility of PFM make it applicable to a wide range of phase transformation phenomena in metallic materials, such as dendrite[9], eutectic[10], peritectic[11], precipitation[12], spinodal decomposition[13], crystal growth[14], dynamic recrystallization and recovery[15], austenite[16], ferrite[17], pearlite[18], bainite[19], martensite[20], and vacancy (irradiation)[21], dislocation[22,23], crack[24], etc.

Parallel to the increase in computer power, advances in computational modeling methods have resulted in a level of sophistication which is comparable to that of experiments. PFM can be integrated or coupled with many advanced atomic scale experimental observations and various computing and intelligent approaches to help design materials and processes more accurately and widely. Figure 2 shows the applicable temporal and spatial scope of the above three PFMs and some applications of integrated PFMs in metallic materials. As this paper aims to summarize the application of integrated PFMs, we will not distinguish the three PFMs in the following.

Some commercial or open-source PF software packages (see Supplementary Note I) have been developed, which greatly promote the wide application of PFM.

Early PFM focused on modeling via setting some phenomenological parameters, gradually developed into quantitatively simulating the materials process matching the spatial and temporal scales of the experiment, which can be achieved by enlarging the interface width[25–28], coupling thermodynamic and dynamic databases[29–32], and distinguishing the crystallographic

[1]Beijing Advanced Innovation Center for Materials Genome Engineering, University of Science and Technology Beijing, Beijing 100083, PR China. [2]School of Materials Science and Engineering, Collaborative Innovation Center of Ministry of Education for High-performance Al and Mg Alloy Materials, North University of China, Taiyuan 030051, PR China. [3]Institute of Materials Intelligent Technology, Liaoning Academy of Materials, Shenyang 110004, PR China. ✉email: zhaoyuhong@nuc.edu.cn

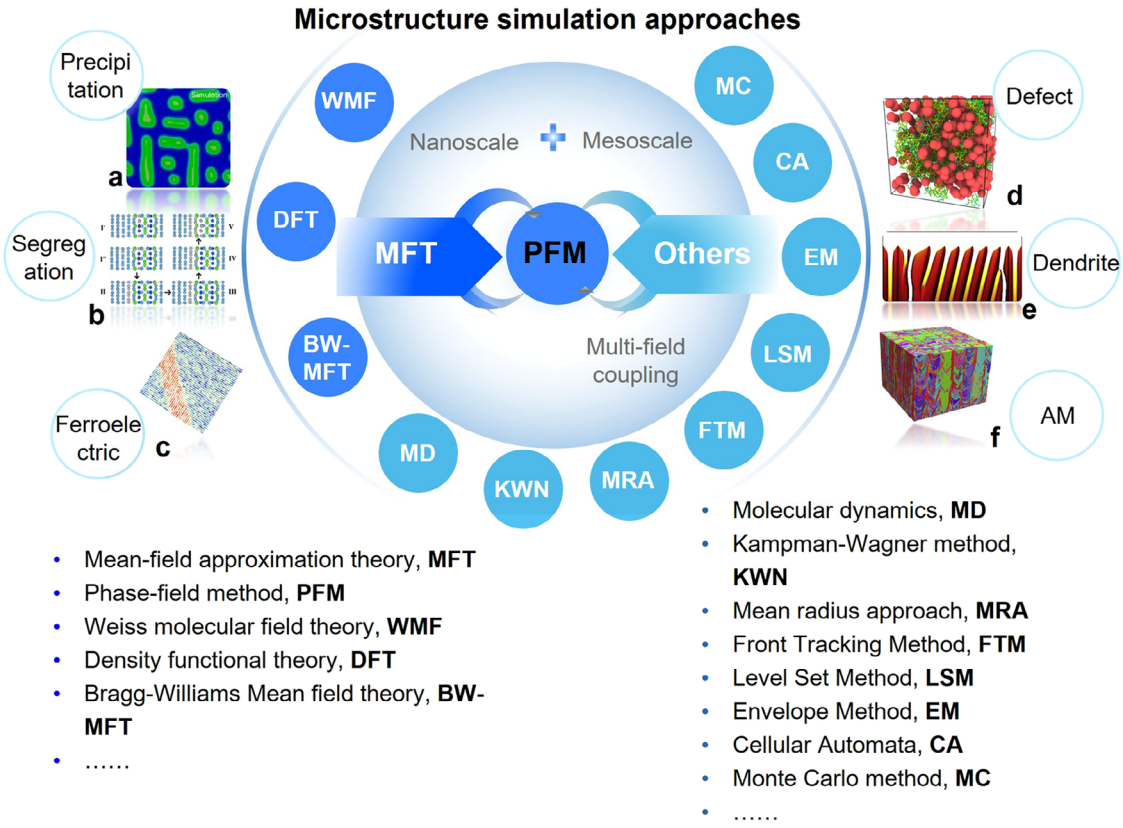

Fig. 1 Commonly used microstructure modeling approaches and some cases. a PF for phase transformation in LA147 alloy[64]. Figure adapted with permission from ref. [64], CC BY 4.0. **b** DFT for Ag-segregation[185]. Copyright Elsevier, 2023. **c** MFT for Ferroelectric phase-transition[186]. Copyright Springer Nature, 2021. **d** MD for virtual voids distribution[187]. Copyright Elsevier, 2021. **e** EM for columnar dendritic solidification[188]. Copyright Elsevier, 2017. **f** CA for additive Manufacturing (AM)[189]. Copyright Elsevier, 2021.

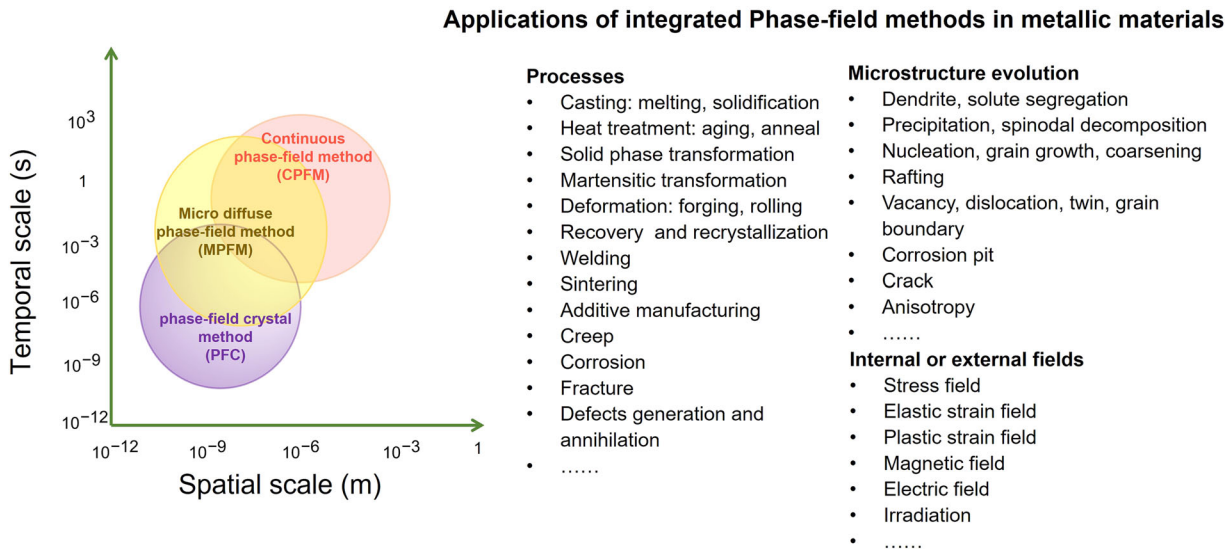

Fig. 2 Integrated computational phase-field theory framework. Schematic of applicable temporal and spatial scope of the three PFMs and some applications in metallic materials of integrated PFMs.

characteristics of different phases[33–35]. Later, researchers paid more attention to helping interpret and understand experimental microstructure by PF simulation. However, it is still an arduous task to optimize the alloy properties and design new materials.

In this brief review, we focus on the potential of integrated PFM in designing high-performance alloys fabricated in process of solidification, precipitation, deformation, or additive manufacturing, etc. In the second section, some recent applications combined with experiments to simulate microstructure evolution are introduced, showing the potential of PFM in quantitatively predicting the relationship between processing and microstructure. In the third part, several key factors, and internal mechanisms

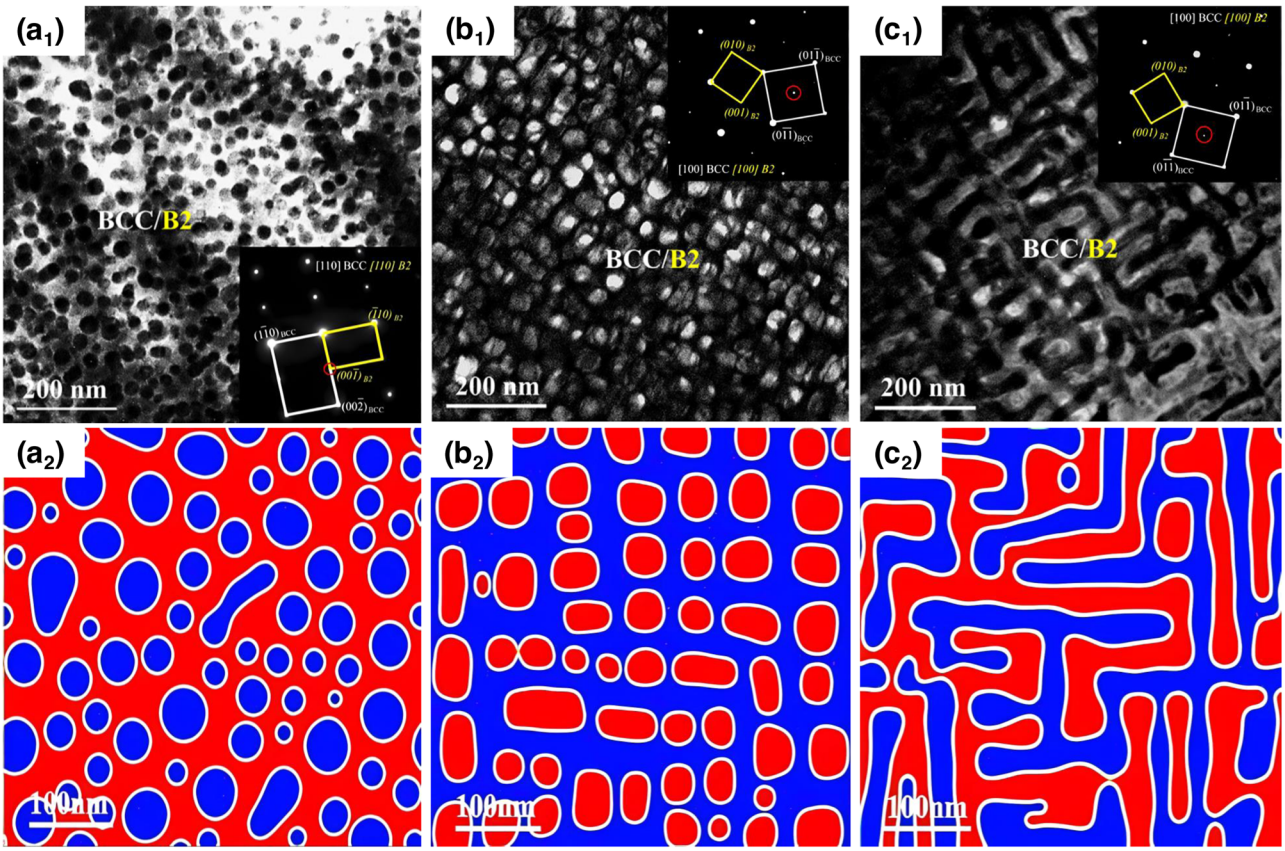

Fig. 3 Microstructure morphology of as-cast HEAs of Al and transition metals (Al-TM) HEAs. ($\mathbf{a_1}$, $\mathbf{b_1}$, $\mathbf{c_1}$) Dark-field TEM images. ($\mathbf{a_2}$, $\mathbf{b_2}$, $\mathbf{c_2}$) Simulated microstructures by PFM. ($\mathbf{a_1}$, $\mathbf{a_2}$) $Al_{21.2}Ni_{29.9}Co_{21.1}Fe_{13.8}Cr_{14.0}$ (No.1-Al21), ($\mathbf{b_1}$, $\mathbf{b_2}$) $Al_{12.5}Ni_{17.5}Co_{17.5}Fe_{17.5}Cr_{35.0}$ (No.2-Al12), and ($\mathbf{c_1}$, $\mathbf{c_2}$) $Al_{17.6}Ni_{20.6}Co_{20.6}Fe_{20.6}Cr_{20.6}$ (No.3-Al17)[54]. Copyright Elsevier, 2020.

to improve alloy properties, especially the PFM design idea, are discussed. The fourth section gives some integrating or coupling ways commonly used in PFM to correlate microstructure and performance, as well as corresponding applications, also several accelerating solutions, such as machine learning and advanced algorithms. The fifth section is the concluding remark and perspective. Finally, the basic theoretical framework of PFM and the coupling path with internal or external fields are briefly summarized.

CROSS VALIDATION OF PHASE-FIELD PREDICTION AND EXPERIMENTAL OBSERVATION

PFM has been applied to a wide variety of material processes as stated in numerous review articles, including solidification[36–39], solid state phase transformation[1,40,41], fracture[42–44], corrosion[45], ferroelectric[46], battery[47], cell[48], etc. This section focuses on the latest application of PFM in comparing and verifying alloy microstructure morphology observed in corresponding experiments[49–53].

Goerler et al.[51] observed topological phase inversion in Ni-based superalloys after long-term aging at 1100 °C for 250h, their corresponding PF simulation indicated that the topological inversion was due to lattice misfit caused by the formation, coalescence and ripening of $\gamma\prime$ precipitates. Besides verifying the morphology and analyzing inherent reason, another case tried to give further pattern criterion. Recently, three typical BCC/B2 coherent microstructures of Al-Ni-Co-Fe-Cr high-entropy alloys (HEAs) were obtained through experiments and PF simulations (Fig. 3)[54], namely spherical, cubic and woven nanoprecipitates, and the elastic mismatch criterion ε>0.4% for cubic precipitate was proposed through PF simulation.

Morphological control can also help formulate technical parameters. Short circuit caused by dendrite growth is a key issue limiting the capacity and longevity of rechargeable battery[55,56]. In 2022, Lin et al.[57] introduced diffusion kinetics, interfacial anisotropy, electric field, stress field and lattice mismatch between deposit and substrate into PFM, so as to reveal the solidification mechanism of three dendrite patterns (needle-like, tooth-like, or tree-like) observed in experiment, as illustrated in Fig. 4. Accordingly, the technology parameters of molten salt electroplating to adjust the dendrite pattern were designed to minimize the failure caused by dendrite growth.

Researchers are no longer satisfied with the cross validation of PF simulation of microstructure morphology and experimental observation, gradually turn attention to seeking the application of PFM in the melting, solidification, aging, rolling and other stages that parts may experience, thus obtaining some relationships between microstructure characteristics and material processing parameters to meet the actual needs of designing high-performance alloys, as described below.

KEY PROCESS FACTORS FOR OPTIMIZING PERFORMANCE

Dendrite arm spacing in solidification

The arm spacing between primary and/or secondary dendrites in as-cast alloys indicates the solute inhomogeneity and segregation in microstructure, which plays a crucial role in mechanical properties of castings[53,58]. Such process parameters as solidification speed, cooling rate, temperature gradient and local solidification time are closely related to the dendrite arm spacing[59]. Bellón et al. quantitatively predicted the stable range of primary dendrite arm spacing (PDAS) in Al-1 wt.%Cu and Al-4

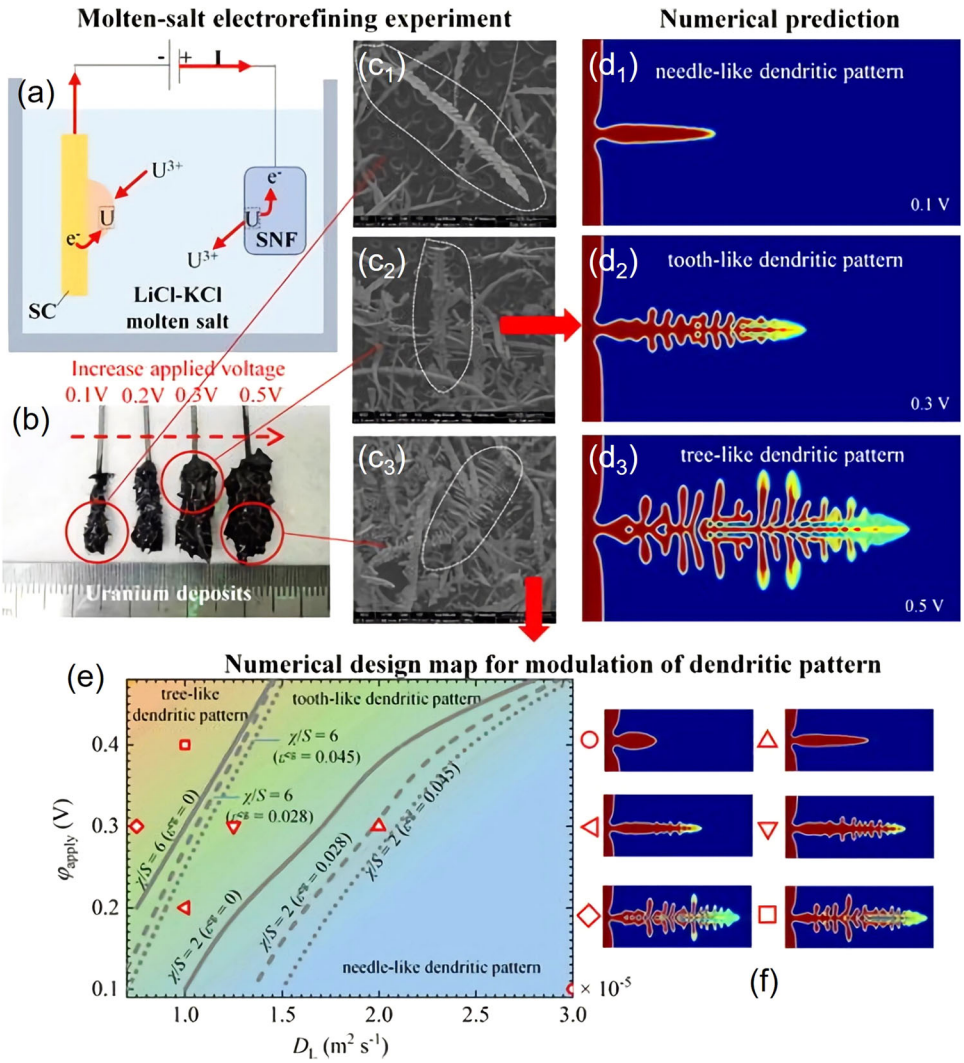

Fig. 4 Comparison of dendrite morphology between simulation and experiment. a Schematic of the electrochemical system. **b** Uranium deposits detached from the cathode. Comparison of molten-salt electrorefining experimental (**c_1**, **c_2**, **c_3**) and PF simulated (**d_1**, **d_2**, **d_3**) dendrite pattern after electrodeposition process of 300 s under different applied voltages. **e** Design for different dendrite patterns with (**f**) dendrites considering varied electric potential, diffusivity, and strain, etc[57]. Copyright Elsevier, 2021.

wt.%Cu alloys[60] using PFM and dendritic needle network method as shown in Fig. 5, and proposed the process parameters to reduce the PDAS and refine the grains, thereby mitigating shrinkage, porosity, cracks and other casting defects.

The above casting defects can be accurately predicted by the macro casting simulation software (EasyCast, ProCast, Novacast, Magma, etc.). Hence, an imperative necessary is to combine meso PF simulation with macro casting software to realize the integrated design from microstructure to defect prediction, and finally to high-performance alloys and structural or functional components.

Early clustering in aging

Generally, as-cast alloys need to undergo heat treatment processes such as homogenization, aging, annealing, quenching, and normalizing, etc. to improve microstructure and properties. Small coherent clustering or Guinier-Preston (GP) zone, precipitated at the earliest quenching or aging stage, is also critical to the mechanical properties of alloys[61]. Both PFC method and MPFM can capture the phase transition details of diffusion time on the atomic scale, which can shed significant light on the elusive fast transformation of the formation, growth and enrichment of early clustering[33]. For instance, Fallah group[33–35,62] elucidated the complete free energy path of early clustering in supersaturated Al-Cu, Al-Cu-Mg, and Al-Mg-Si alloys with PFC, found that dislocations (Fig. 6) can significantly reduce the energy barrier height and the critical nucleation size, resulting in higher aggregation rate and finer clusterings[34,62].

Additionally, the following specific phase separation mechanism leading to microstructure diversity containing various defects, always plays a significant role in affecting materials performance.

Spinodal decomposition (SD) in precipitation

Compared with the nucleation and growth mechanism (NG), the most prominent difference of SD is that no nucleation energy barrier is required[63]. Xin et al.[64] designed an SD strengthened ultralight high-strength Mg-14Li-7Al (LA147, wt.%) alloy by using experiments and PF simulation, and its specific yield strength (470-500 kNmkg^{-1}) almost exceeds that of all other engineering alloys. As shown in Fig. 7, PF simulation not only provides direct evidence of $D0_3$-Mg_3Al ordered phase precipitated by SD, but also quantitively determines the amplitude modulation wavelength of three stages in SD, i.e., incubation period, rapid growth period, and equilibrium period. Subsequently, they further explored the precipitation mechanism and sequence in Mg-11Li-3Al alloy[65], in

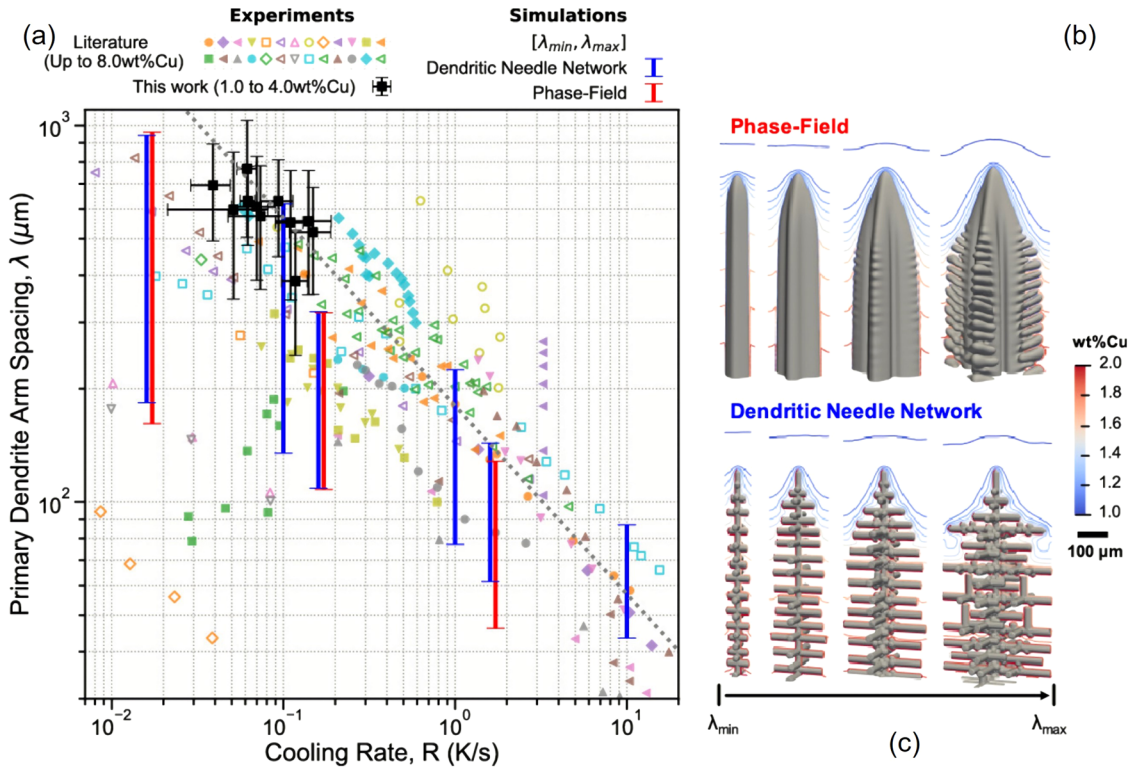

Fig. 5 Primary dendrite spacing in cast metallic alloys[60]. a PDAS as a function of cooling rate for Al-1wt.%Cu alloy. The dendrite morphology from (**b**) PFM and (**c**) dendritic needle network model. Copyright Elsevier, 2021.

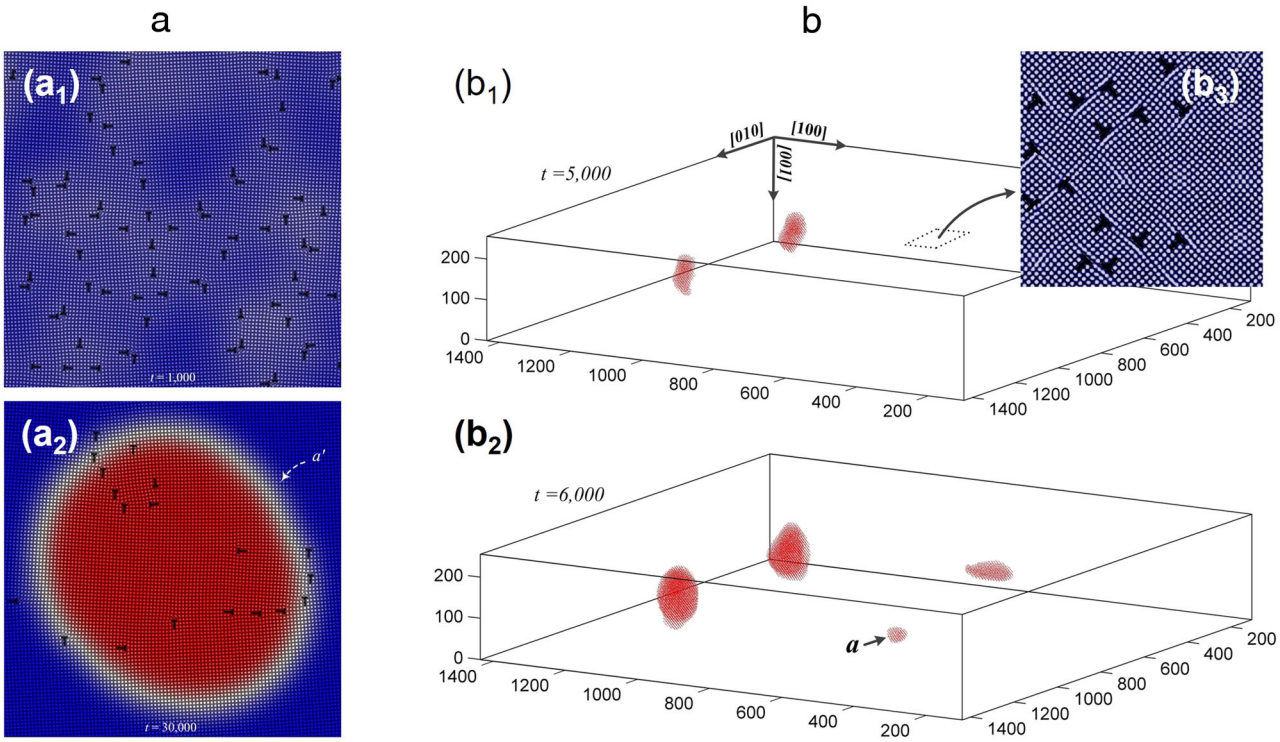

Fig. 6 PFC simulation for the evolution of Cu-rich clusters. a Formation and evolution of 2D Cu-rich clusters, (**a**$_1$) $t = 1000$ and (**a**$_2$) $t = 30000$. The system undergoes a process of rearrangement and/or annihilation of dislocations within the matrix, leading to the formation of cluster *a*[62]. Copyright Elsevier, 2013. **b** Evolution of 3D Cu-rich clusters, (**b**$_1$) $t = 5000$ and (**b**$_2$) $t = 30000$. The black T-like symbol in the inset of (**b**$_3$) represents edge dislocation[34]. Copyright Elsevier, 2016.

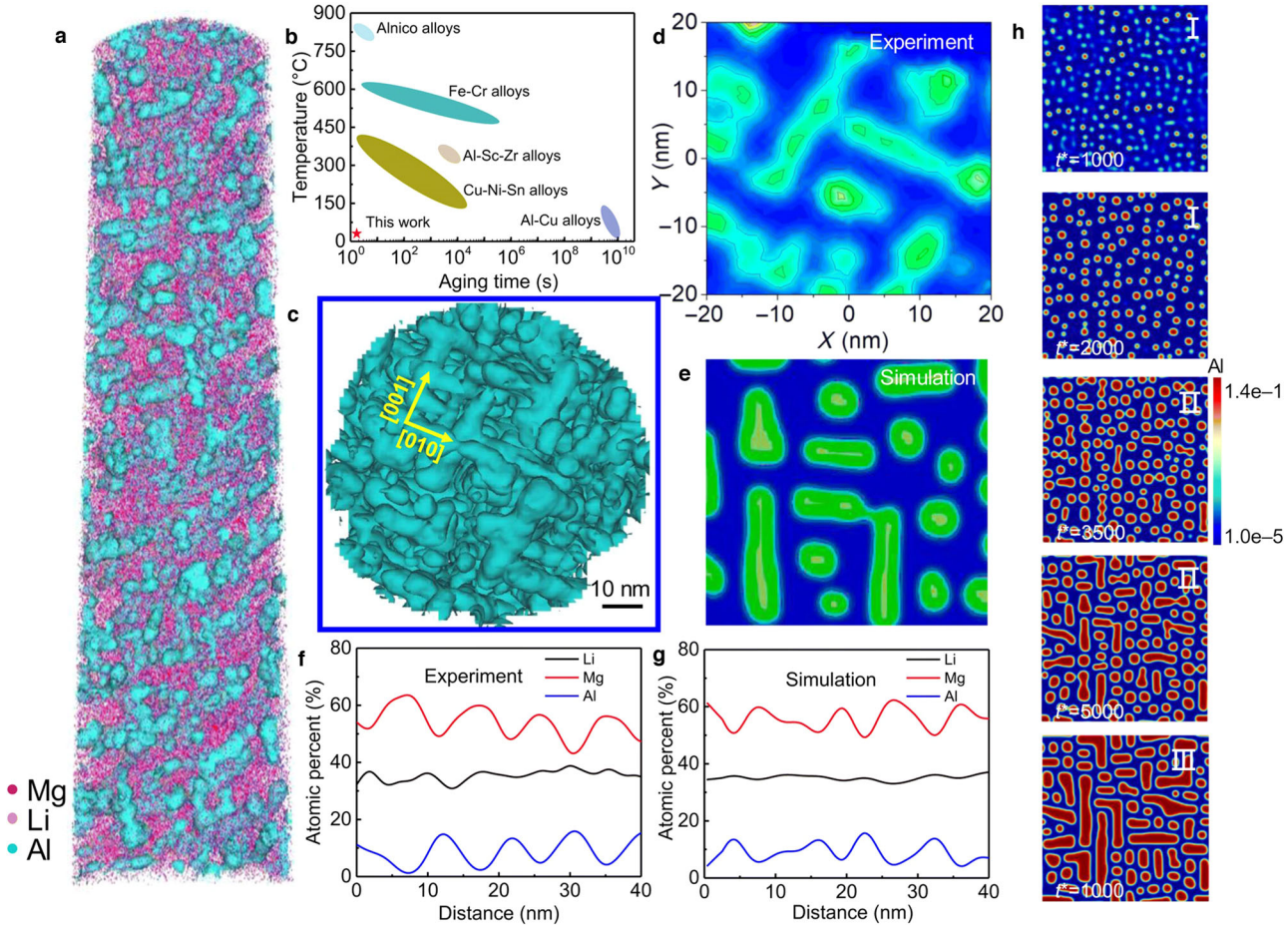

Fig. 7 The atom probe tomography (APT) results and PF simulation of water-quenched LA147. a Reconstructed APT volume showing Al-rich zones (blue phase) distributed within the BCC phase (magenta phase) (plotted with 6 at % Al iso-surface). **b** Time-temperature transformation diagrams of LA147 and a range of spinodal alloys. **c** The bottom view of the extracted Al-rich zones in **a** shows the characteristic morphology and crystallographic features of a classic spinodal decomposition. **d**, **e** Composition maps were generated from the APT data and PF simulation, respectively. **f**, **g** One-dimensional concentration profile of Mg, Li, and Al through the Al-rich zones in **d** and **e**, respectively. **h** PF simulation of microstructure evolution of Al-rich region[64]. Figure adapted with permission from ref. [64], CC BY 4.0.

which the PF simulation reproduced the evolution mechanism from θ ($D0_3$-Mg_3Al) phase to Al-Li phase with core-shell structure after medium temperature (270 °C) aging, and predicted the corresponding hardness.

The microstructures generated by SD or NG mechanisms usually work under different temperatures, stress, or other load conditions, which may form various point defects, line defects and surface defects, and have a serious impact on alloy properties. Currently, PF simulation plays an increasingly important role in alloy design considering defect formation and evolution.

Defects of twins and dislocations during deformation

Nanotwins can improve the work hardening rate of metallic materials[66,67], which is mainly due to the interplay between dislocations and twins, including de-twinning[68,69], dislocation crossing twin boundary[70] and twin boundary steps becoming dislocation accumulation site or dislocation sources[71,72], etc. PFC[73] is an effective tool for intuitively revealing the interaction between nanotwins and dislocations during equal volume deformation of rolling, forging, or Split-Hopkinson-Pressure-Bar. Here, strain rate $\dot{\varepsilon}<10^{-7} \sim 10^{-2}\, s^{-1}$ is applied to avoid calculation divergence.

For example, a new $Cu_{92}Al_5Ni_3$ (wt.%) alloy[74] with tensile strength of 797.06 Mpa and elongation of 28.66% was designed through melting-aging-deformation processes. PF simulation showed that the interplay between twins and dislocations led to such high performance, as shown in Fig. 8, including twin boundary fragmentation, formation/annihilation of dislocation dipoles, and climbing-slipping motion of dislocations. The typical characteristics of high strength-ductility Cu alloys, such as fine grains, high twin density and stable grain boundaries, were also proposed.

Defects of Void and bubble expansion

PFM is also used to predict the evolution of bubbles and voids during irradiation, to calculate local thermodynamic properties, and to evaluate the microstructure effect on the properties of metallic materials[75]. For example, Hu et al.[76] put forward the concept of effective thermal conductivity K_G, employed the heat transport equation and PFM of polycrystalline U–Mo fuel alloy with a given crystal morphology and gas bubble distribution to calculate the thermal conductivity of heterogeneous systems, Fig. 9 illustrated the effect of bubbles between and inside particles on K_G.

Diffusionless martensitic transformation

The diffusionless martensite transformation is often accompanied by high strength and hardness, e.g., the tensile strength of martensitic steel is within 600 MPa~1600 MPa. Shchyglo et al.[77] found that when the carbon content increased from 0.1% to 0.3%, the yield strength of lath martensitic low-carbon steel increased by 45.83%,

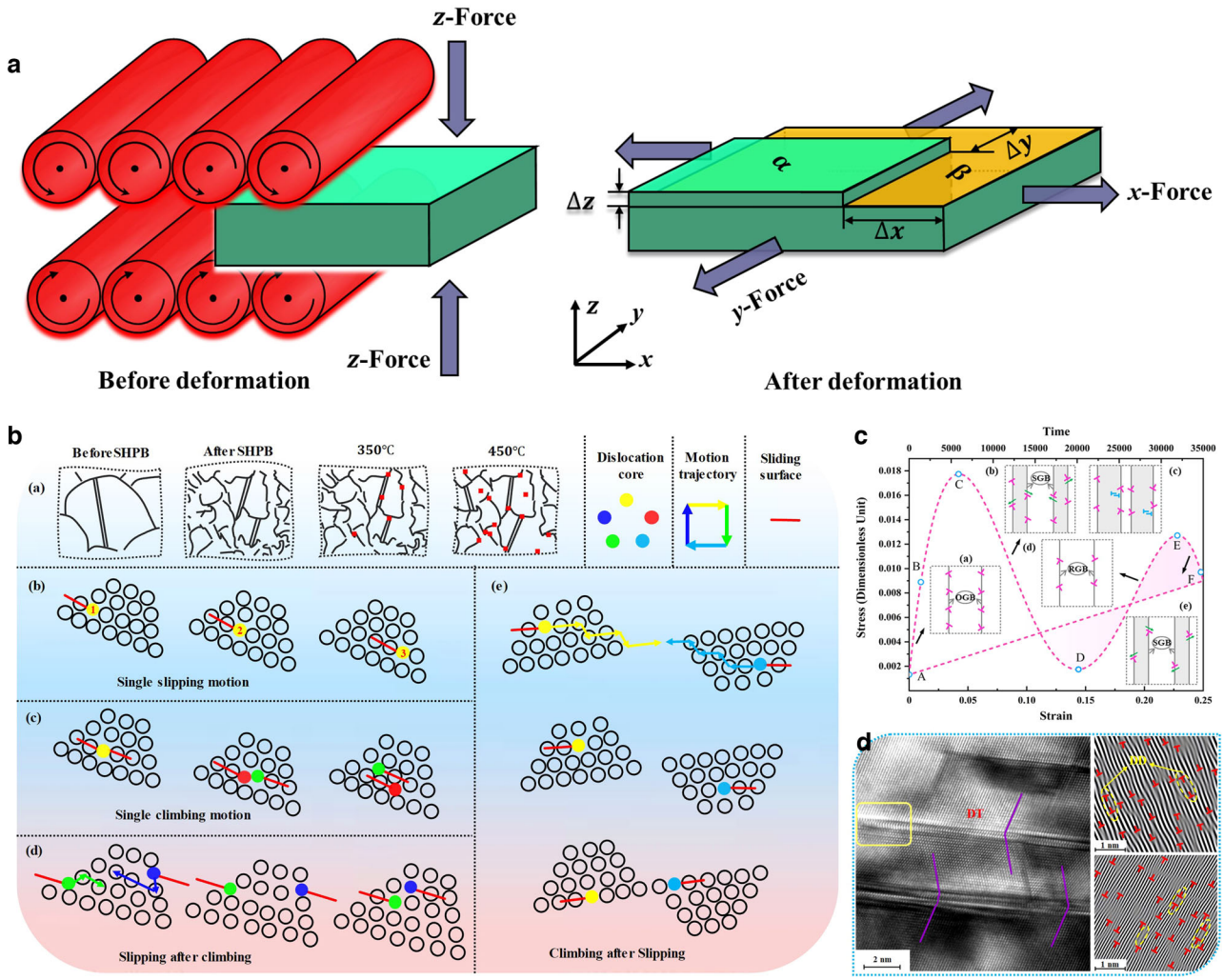

Fig. 8 Twining/grain boundaries optimization mechanism[74]. a Schematics of equal volume deformation. **b** Microstructure under different processing methods. **c** Stress-strain curve, (a-e) is the schematic of original grain boundaries (OGB), sub-grain boundaries (SGB), and recrystallized grain boundaries (RGB), respectively. **d** High-Resolution-Transmission-Electron-Microscope (HRTEM) image of deformation twin (DT) and the inverse Fast Fourier transform (IFFT) image of yellow frame area. Copyright Elsevier, 2022.

which can be attributed to displacive martensitic transformation. However, due to the extremely rapid formation of martensite, it is almost impossible to experimentally capture the nucleation and growth of martensite in steel. Therefore, they proposed a martensite PFM considering 24 K-S variants to reveal the process from nucleation to final complex microstructure (as shown in Fig. 10), and clarified the martensite strengthen mechanism.

Additionally, martensite transformation of Ni-Ti-based shape memory alloys[78,79] and the tetragonal to monoclinic transition of Zr alloys[80,81] are also investigated by PFM.

INTEGRATING AND CORRELATING PERFORMANCE MODELS

The aforementioned PFM design scheme is effective by comparing the morphology and associating the actual process parameters. How to directly, accurately, and efficiently design high-practical service performance alloys using PFM is a more urgent issue. Here we concisely summarize several integrating and correlating ways and prominent applications: (I) empirical models, (II) machine learning, (III) advanced algorithms, (IV) coupling with discrete models of continuum system, (V) integrating with macroscopic constitutive equations, and(VI) optimizing process parameters.

Empirical models correlating with performance

Introducing microstructure data from extensive experiments or PF simulations as variables into empirical models can characterize the microstructure evolution, and obtain mechanical response, thus improving the efficiency of screening high-performance materials.

Geometric hardening parameter. The critical stress σ_c of crack initiation in mushy zone of Fe-C alloy is related to the geometric hardening parameter η caused by the interdendritic contact area[82],

$$\sigma_c = \eta \cdot \left[{}^{\delta}f_s\sigma_c^{\delta} + {}^{\gamma}f_s\sigma_c^{\gamma}\right] \quad (1)$$

where σ_c^{δ} and σ_c^{γ} are the flow stress of δ-phase (Fe-0.11wt.%C) and γ-phase (Fe-0.60 wt.%C). ${}^{\delta}f_s$ and ${}^{\gamma}f_s$ are the solid fraction of δ-phase and γ-phase. From Lee and Kim's yield criterion for porous metals[83], the geometric hardening parameter η is proposed as the function of solid fraction[84],

$$\eta = \frac{L}{\lambda} = \left[\frac{f_s - {}^{c}f_s}{1 - {}^{c}f_s}\right]^{a} \text{ at } 0 < {}^{c}f_s \le f_s \le 1 \quad (2)$$

where f_s, ${}^{c}f_s$ represent the solid fraction and critical solid fraction in the mushy zone respectively. a is a constant. L and λ are the primary

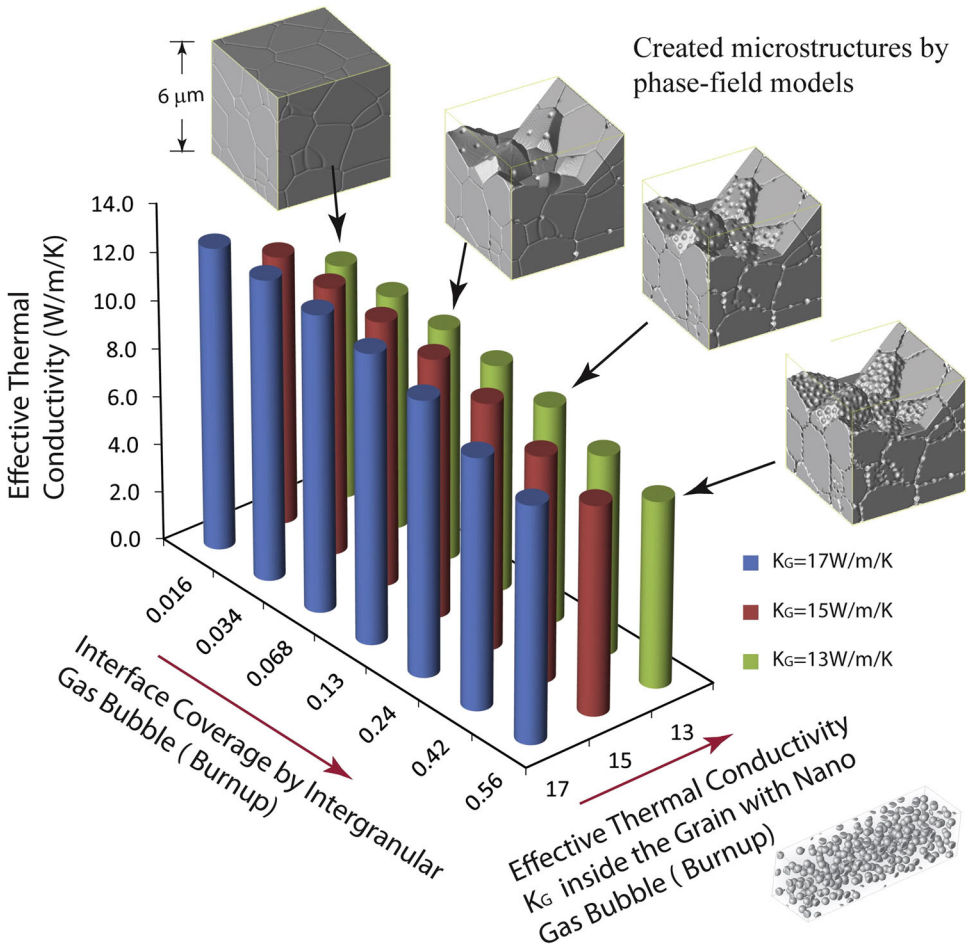

Fig. 9 Effective thermal conductivity of polycrystalline materials as a function of interface coverage of intergranular gas bubbles and effective thermal conductivity KG of grains with nano-sized intragranular gas bubbles[76]. Copyright Elsevier, 2015.

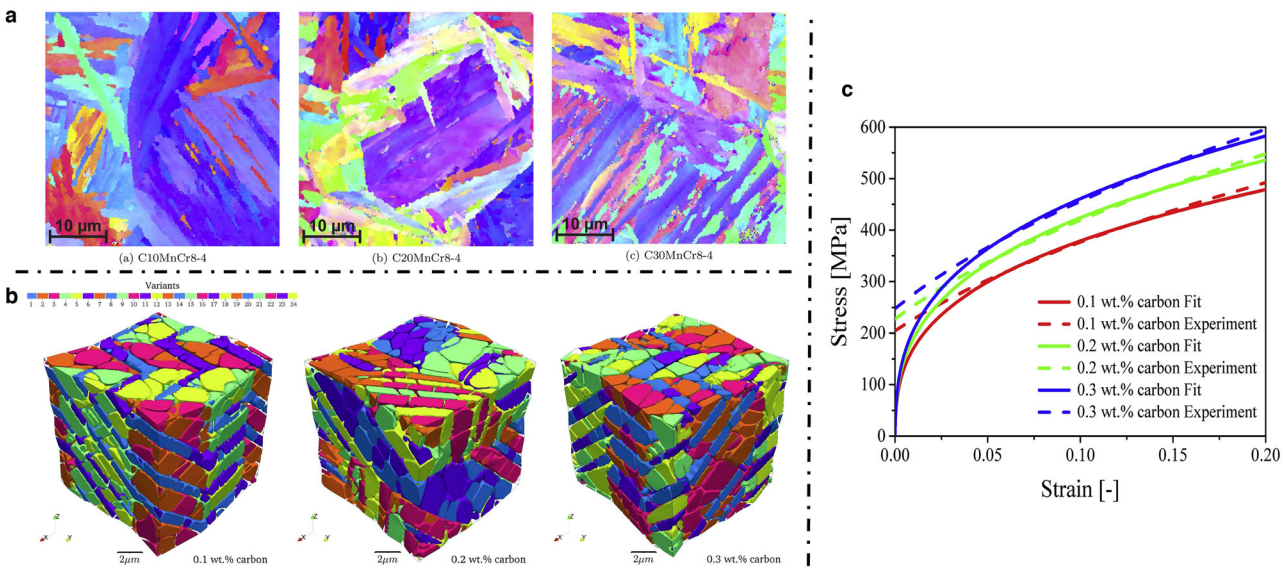

Fig. 10 Simulation vs experiment of martensite in samples containing 0.1, 0.2, and 0.3 wt.% carbon[77]. a EBSD images. **b** PF simulations. **c** Stress-strain curves. Copyright Elsevier, 2019.

arm spacing and contact length in Fig. 11a. Seol et al.[84] quantified the effect of dendrite morphology on mechanical strength of carbon steel using PFM to calculate the contact ratio (L/λ) in Fig. 11b, found that strength of $a = 1.5$ is more consistent with measured data in Fig. 11c.

Comprehensive evaluation function. Based on the microstructure information obtained from 10 sets of 3D PF simulations and 40 sets of experiments, taking the phase-fraction, grain-size, and shape- factor of γ′ precipitate as evaluation indicators,

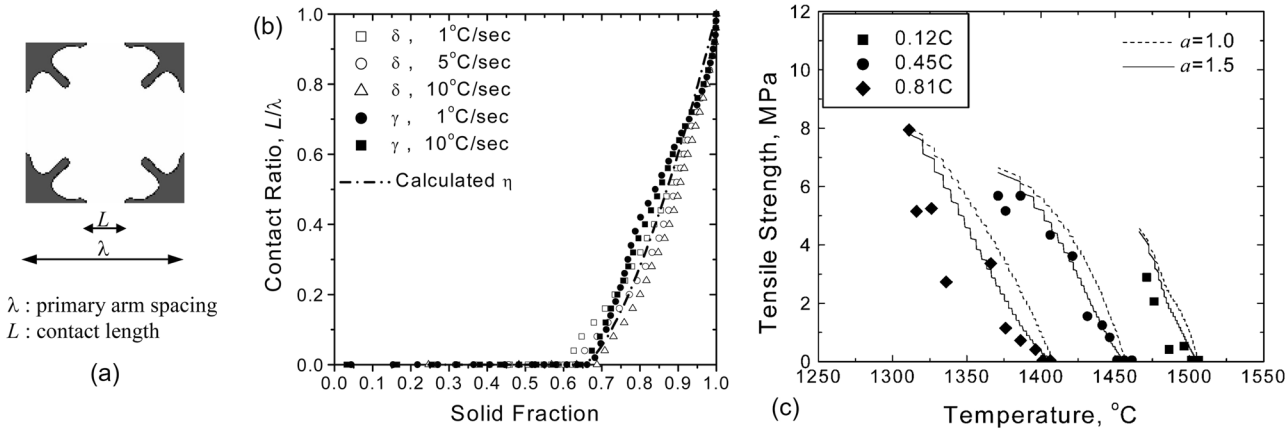

Fig. 11 Effect of dendrite morphology on tensile strength. a The contact ratio L/λ. **b** Contact ratio L/λ as a function of solid fraction during solidification of δ and γ phases with various cooling rates. **c** Critical fracture strength in the mushy zone with different carbon content. Marks and curves indicate the tensile strength of simulation[84] (Copyright Elsevier, 2016). and experiment[82], (Figure adapted with permission from ref. [82], CC BY 4.0.) respectively.

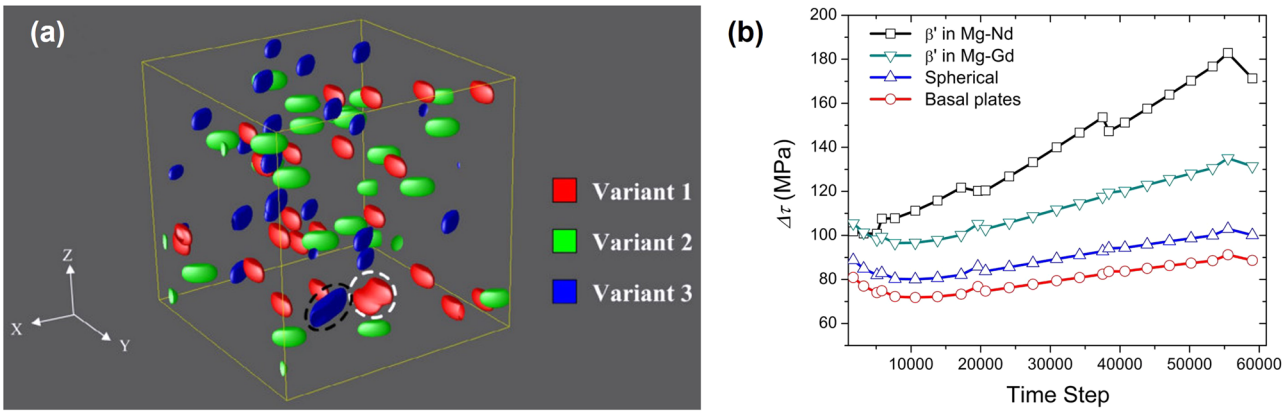

Fig. 12 Prediction of ΔCRSS in Mg-RE alloy[88]. a 3-D morphology of multi-β' particles simulated by PFM. **b** Evolution of CRSS for systems containing β' precipitates with different shapes. The volume fraction of β' precipitates reach equilibrium (4.8%) at about $t^* = 55,000\Delta t$. Copyright Elsevier, 2014.

Ta et al.[85] proposed an evaluation function (3) to select the best composition and heat treatment schedule, and found Ni-19.36 at.% alloy had the best mechanical properties aging at 973 K for 100000 s. The following linear comprehensive evaluation function is established by empowering weight w_1, w_2 and w_3 to different indicators[85],

$$\begin{aligned}\text{Composite indicator} = w_1 \times \text{Phase\_fraction} + w_2 \times \text{Grain\_size} \\ + w_3 \times \text{Shape\_factor}\end{aligned} \quad (3)$$

where w_1, w_2 and w_3 are the weight factor of phase volume fraction, grain size, and geometric shape of γ' precipitates, respectively. The evaluation function represents the quality of alloy performance.

Critical resolved shear stress increment. For shear-resistant precipitates, dislocations are difficult to cut through, and often bypass the precipitates by Orowan mechanism, leaving dislocation loops around the precipitates to block dislocation motion[86]. The precipitation behavior of Mg-Re alloy during non-isothermal aging was studied by PFM, the critical resolved shear stress (CRSS) increment caused by Orowan loop for spherical and plate-shaped precipitates was given by $\Delta\tau_s$[87] and $\Delta\tau_p$[88], respectively,

$$\Delta\tau_s = \frac{\mu \cdot G\mathbf{b}}{2\pi M \cdot \lambda_r} \ln\left(\frac{R}{r_0}\right) \quad (4)$$

$$\Delta\tau_p = \frac{G\mathbf{b}}{2\pi\sqrt{1-\nu}(0.825\sqrt{\frac{d_t t_t}{f}} - 0.393 d_t - 0.866 t_t)} \times \ln\frac{0.866\sqrt{d_t t_t}}{\mathbf{b}} \quad (5)$$

where μ is the ratio of CRSS values of the alloys containing random or regular distributed precipitates, λ_r is the spacing between particles that have a regular distribution, G is the shear modulus of Mg matrix, $\mathbf{b}$ Burgers vector of the slip dislocations, $M = (1-\nu)^{\frac{1}{2}}$ is a constant, ν the Possion's ratio, R and r_0 the outer and inner cut-off radius of the dislocation. f the volume fractions of $\beta\prime$ precipitates, d_t uniform diameter of prismatic plates, t_t represents mean planar thickness of prismatic plates. Using Eq. (5), the physical parameters of metastable $\beta\prime$ precipitates calculated by PFM can be used to predict ΔCRSS in Mg-Re alloys[88], as shown in Fig. 12. It was also found that the hardening effect of Mg-Nd alloy is more significant than that of Mg-Gd alloy with the same volume fraction of $\beta\prime$ precipitates.

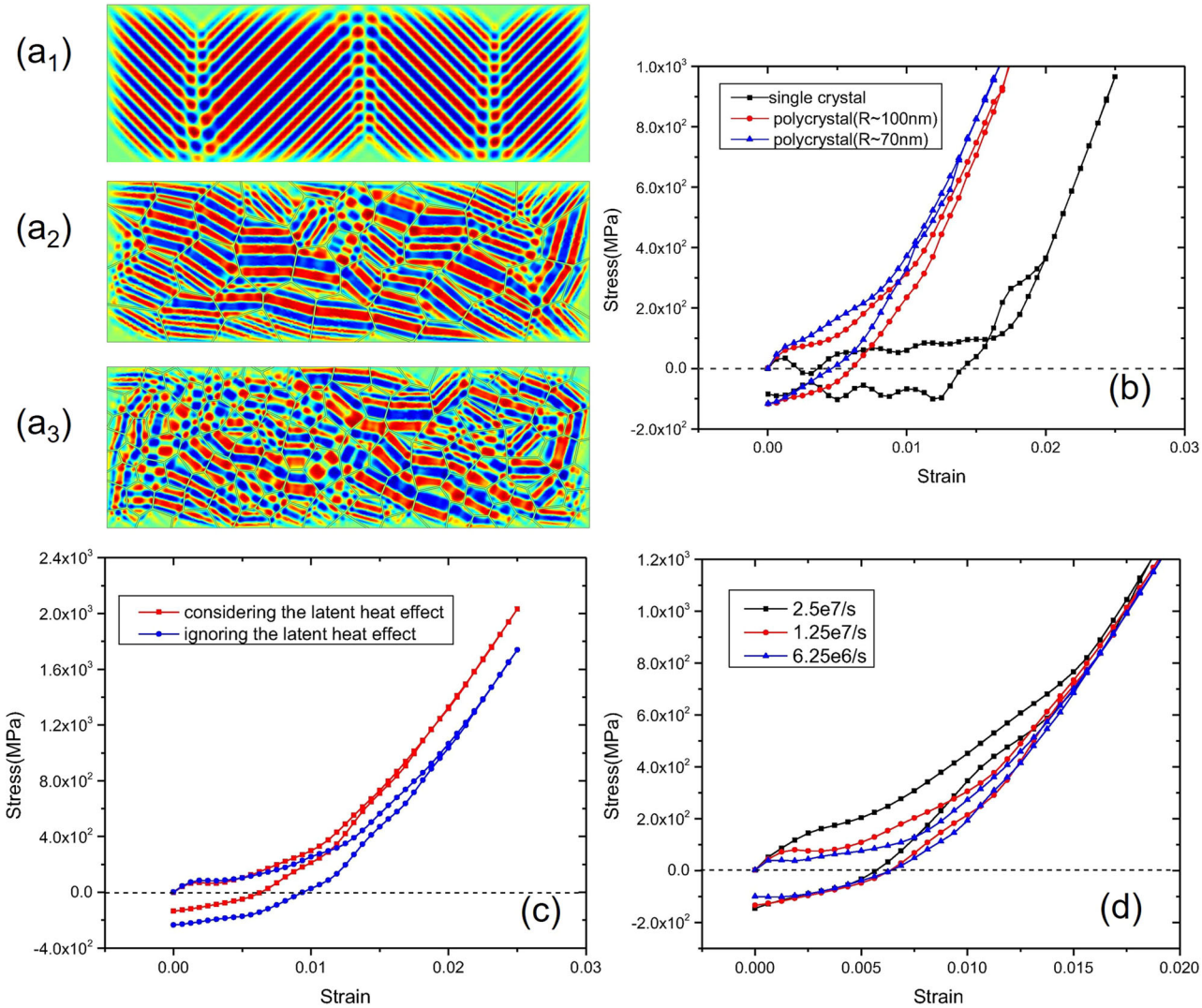

Fig. 13 The stress-strain response in different environments[89]. The PF simulated microstructure patterns of single crystalline nanowire ($\mathbf{a_1}$) and polycrystalline nanowires with different grain sizes ($\mathbf{a_2}$) R~100 nm and ($\mathbf{a_3}$) R~70 nm. Stress-strain curves of **(b)** the single crystalline nanowire and polycrystalline nanowires with different grain sizes at temperature below T_m, (**c**) the latent heat effect, and (**d**) grain size R~ 100 nm with different strain rates. Copyright Elsevier, 2018.

Strain rate hardening effect. The unique thermomechanical properties of shape memory alloys are due to martensitic transformation induced by temperature or stress, the correlated stress-strain relation is[89],

$$\sigma_{ij}(\boldsymbol{r},t)=\frac{\delta F}{\delta\varepsilon_{ij}(\boldsymbol{r},t)} \tag{6}$$

where σ_{ij} is the stress tensor, δ the variation operator, $F=F_{\text{che}}+F_{\text{el}}+F_{\text{grad}}$ is the system total free energy, and F_{che}, F_{el} and F_{grad} are the chemical free energy, elastic strain energy and gradient energy, respectively. $\varepsilon_{ij}=(\partial u_i/\partial \boldsymbol{r}_j+\partial u_j/\partial \boldsymbol{r}_i)/2$ is Cauchy-Lagrange strain tensor, and u_i, $i=1, 2$ is the displacement in x or y direction[90]. Using strain and temperature as order parameters[81], the PF approach can be extended to describe thermomechanical equilibrium process. Ahluwalia et al.[91] investigated the dependence of martensitic transformation and stress-strain response on grain size in nanocrystalline shape memory alloys, discussed grain size, latent heat effect and loading rate[89], as illustrated in Fig. 13, showing that polycrystalline nanowires, latent heat, and higher strain rate can induce strain rate hardening effect.

Integrating with machine learning

The number of microstructural and compositional parameters, processes, and configurations to combine to invent a new material is enormous. Compared with traditional physical methods, using machine learning (ML), we can directly face the required performance, avoid interwinding in physical and chemical processes, and efficiently and quickly design new materials or optimize manufacturing process of existing materials in a cross-scale manner. The ever-increasing computational resources and development of advanced ML models such as reinforcement learning[92], Gaussian process regression[93], and many other numerical algorithms make ML-PF modeling a rapidly growing topic[94–97]. Its main strategies can be roughly summarized as follows: (1) generating datasets by PFM to construct neural networks[96,98], (2) using ML technology to build a fast and reliable surrogate model of PFM[99–104], (3) extracting key microstructure information from PFM to generate image datesets[105–107], and (4) integrating machine-learned functions or parameters (e.g. free energies, partial differential equations, mobilities) as a model[101,108,109] for PFM. Yet, the size and uncertainty of training

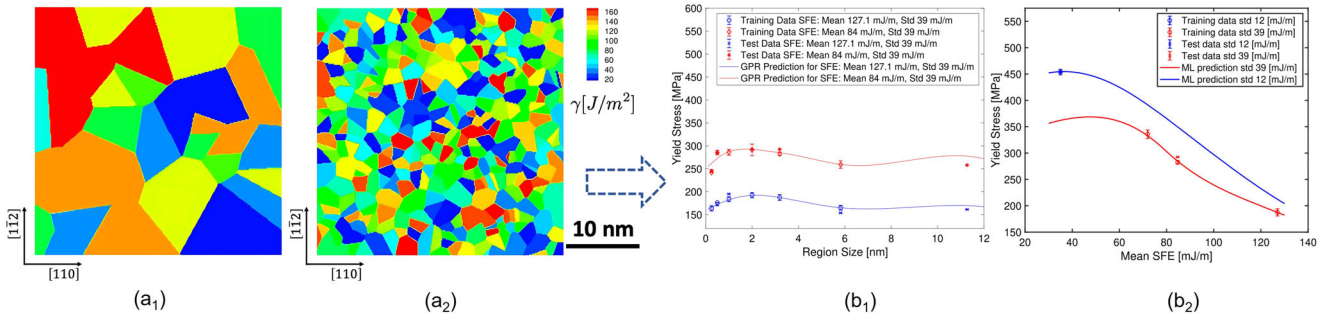

Fig. 14 Example of phase-field coupling machine learning[111]. (**a$_1$, a$_2$**) Two examples of the random stacking fault landscape simulated by PFM. (**b$_1$, b$_2$**) Gaussian Process Regression (GPR) prediction of yield stress as a function of region sizes and SFE. Copyright American Society of Mechanical Engineers (ASME), 2021.

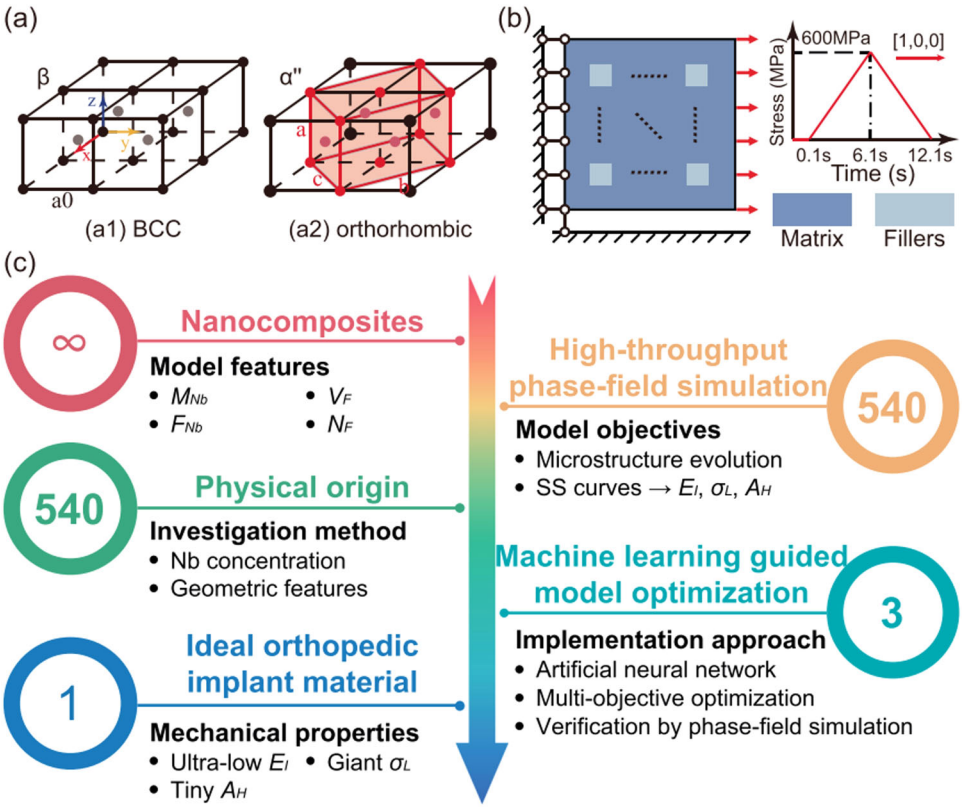

Fig. 15 Computational framework for the design of the Ti-Nb nanocomposite. a Crystal structure of **(a$_1$)** BCC parent and **(a$_2$)** martensitic (orthorhombic) phase. **b** Square-array distributed Nb-lean nanofillers in the Ti-Nb nanocomposite and loading-unloading condition and profile. **c** High-throughput PF simulation framework for the Ti-Nb nanocomposite. Details in ref. [97]. Figure adapted with permission from ref. [97], CC BY 4.0.

data, the selection of training metrics, and the balancing of accuracy, interpretability and versatility are still difficult tasks[110].

Here, we list several promising examples of accelerating or innovating metallic systems design via PFM coupled with ML code, which is a critical knowledge gap and one of the research directions worth expanding in the future.

From microstructure to performance. Predicting material properties from their microstructure is an active research field in ML field.

In 2021, Vilalta et al.[111] used PF dislocation dynamics simulation to obtain different stacking fault energy (SFE) distributions of Ni-Co-Fe-Cr-Mn family HEAs, and input them into the ML model as learning data to predict the relationship between yield stress and SFE, with an error of about 2%, as shown in Fig. 14 (b$_1$-b$_2$), showing that for a given SFE, the yield stress increases slightly in the size between 1 nm and 4 nm, and the critical yield stress has a peak between the mean SFE of 40 mJ/m~50 mJ/m.

From performance to microstructure reversely. Reverse design for specific performances can optimize alloy microstructure or processing history more efficiently and accurately.

Zhu et al.[97] proposed a performance-oriented concentration modulation approach to achieve the extraordinary mechanical properties of Ti-Nb shape memory alloys, the computation framework is shown in Fig. 15. To seek optimal microstructure, the high-throughput PF simulations, yielding 540 candidates, were conducted using four microstructure feature variables, namely, Nb concentration of the matrix (M_{Nb}) and nanofillers (F_{Nb}), volume fraction of nanofillers (V_F), and the number of nanofillers (N_F). The perfect combination with ultralow modulus ($E_I = 16.05$ MPa),

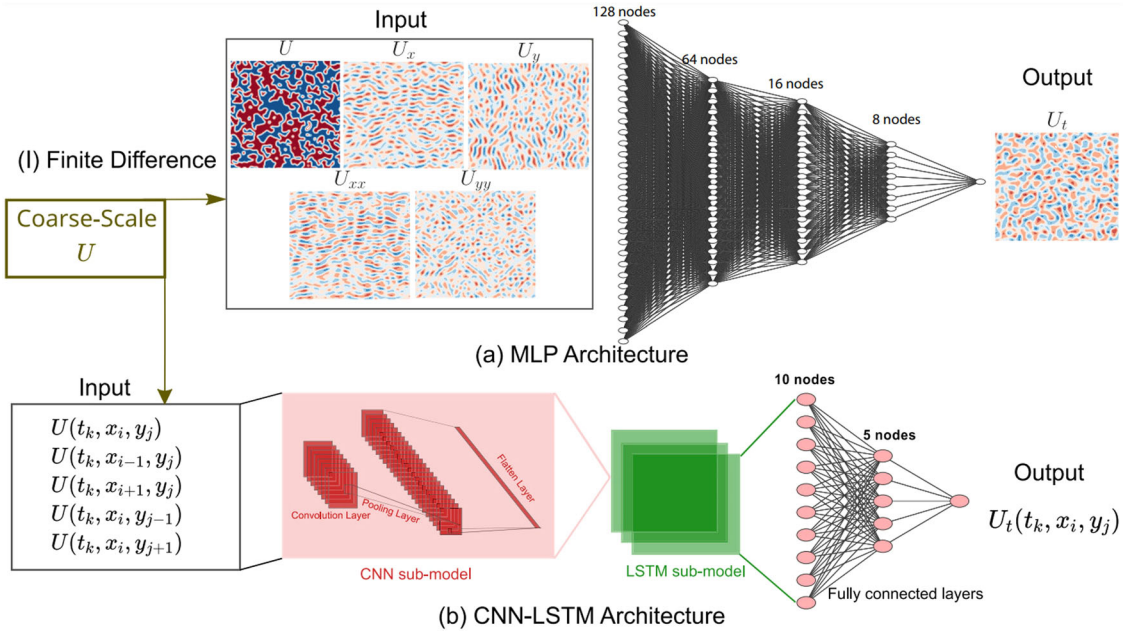

Fig. 16 Schematic of the general steps in the discovery of PDEs with spatial derivatives dictionary[109]. 2022. **a** A MLP architecture and **b** A CNN-LSTM for learning coarse-scale PDEs. Copyright American Physical Society.

quasi-linear elasticity ($\sigma_L = 468.40$ MPa), and near zero stress-strain hysteresis is screened by coupling ML, i.e., $M_{Nb} = 18.4\%$, $V_F = 25\%$, $F_{Nb} = 7.2\%$, $N_F = 16$.

Some machine learning techniques accelerating PF simulation. With the ever-increasing computing resources and development of advanced machine learning algorithms, the strategy of "machine learning-phase field method" has an extremely broad application prospect[112]. So far, this strategy mainly focuses on the identification of microstructure evolution diagrams and accelerates the solution of partial differential equations (Allen-Cahn and Cahn-Hilliard equations). Deep Neural Network (DNN) including Convolutional Neural Network (CNN) and Recurrent Neural Network (RNN) has paved the way for identification of microstructure evolution diagrams. Notably, such RNN or its subclass of Long-Short Term Memory (LSTM) has been proved to be successful in rapidly predicting the time evolution of the microstructure. On the other hand, Physics-Informed Neural Network (PINN) and Deep Operator Network (DeepONet), as the general neural network framework of the dynamic system governed by the free energy functional gradient flow, provide a promising method for the efficient solution of partial differential equations coupled physical field information.

RNN and LSTM: RNN can preserve past information and handle temporal dependencies, i.e., the history of microstructure evolution[113]. In this way, phase-field simulations can be redefined as multivariable time-series problem[99,113,114]. In order to overcome the shortcoming of vanishing or exploding gradients that often exist when using RNN, LSTM is proposed as a subclass of RNN, which has better accuracy and long-term predictability, also can predict next frame. Compared with the original phase-field simulation, the accelerated phase-field framework with LSTM can not only maintain the same accuracy, but also accelerate the prediction speed at least three orders of magnitude[113]. Figure 16 is a schematic diagram of multilayer perceptron (MLP) and convolutional neural network and long short-term memory (CNN-LSTM) architecture for discovering partial differential equations (PDEs) with spatial derivatives dictionary. Relevant researches continue to emerge, including brittle fracture[115,116], spinodal decomposition[99], single dendrite growth[116] and polycrystalline grain formation[117], etc.

DeepONet and FNO: In 2019, Brown University proposed a DeepONet that uses operators to solve partial differential equations (PDEs), which is unique in that it has two parts: branch and trunk. Some operators are generated by branch network learning to approximate the input data, while the trunk network is responsible for the output data. Finally, the data from the two networks are introduced into DeepONet to solve the PDEs. DeepONet is one of the possible ways to learn phase-field-free energy functional solution operators from the labeled input-output datasets in high-dimensional systems (e.g., multiple phases, scales, and physical fields). This architecture is capable of learning the mapping of field variable distribution from the current time step to the next time step[118]. According to statistics, compared with traditional high-fidelity phase-field simulation, the framework integrating a convolutional autoencoder architecture with a DeepONet would save 135 minutes for each evolution. DeepONet has been applied to research crack path in quasi-brittle materials[119] and spinodal decomposition of a two phase mixture[120], etc.

Another simpler architecture called "Fourier neural operator (FNO)" developed by California Institute of Technology can dramatically speed up the solution of PDE by using many Fourier layers. In an example of solving Navier-Stocks (N-S) equation, 30,000 simulations are needed, FNO solution time is less than one second, and DeepONet takes 2.5 seconds, while the traditional solver takes 18 hours[121]. Then, they presented an enhanced Fourier neural operator, named U-FNO, that combines the advantages of FNO-based and CNN-based models to provide results for PDEs that are both highly accurate and data efficient[122]. Now, FNO and U-FNO have been successfully used to solve N-S equations of single-phase or multiphase flows. Therefore, it is very promising to use DeepONet or FNO/U-FNO architecture to solve the Allen-Cahn or/and Cahn-Hilliard equations of PFM.

Genetic algorithms: Genetic algorithm is a random search method, which can converge to a global minimum value of the objective function[123]. Using genetic algorithms to solve optimization problems includes problem coding, generation of initial

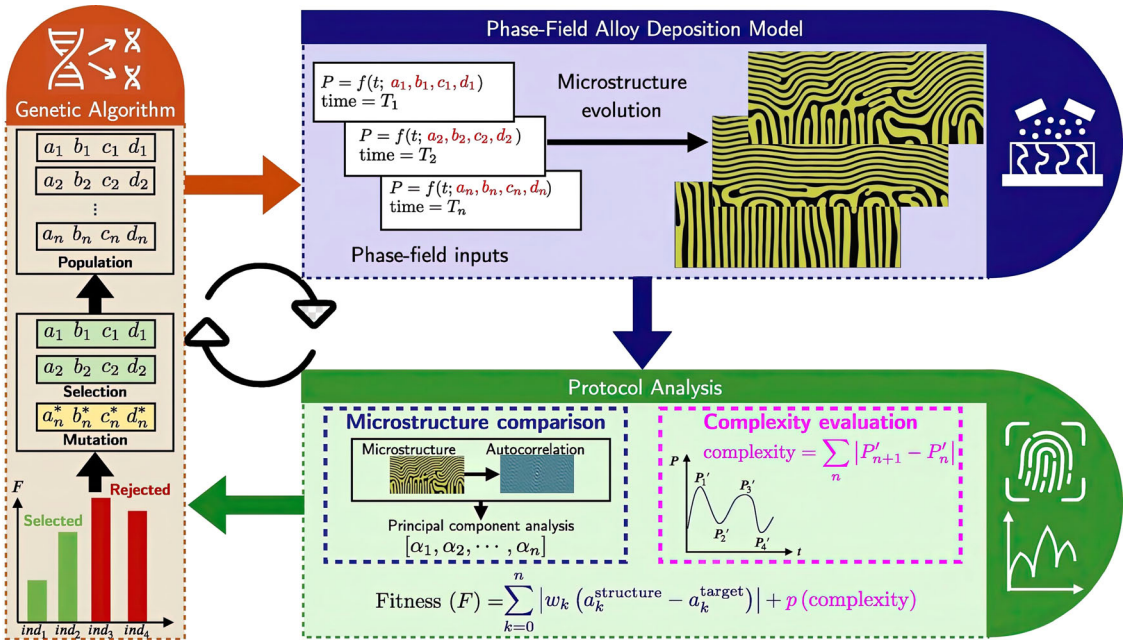

Fig. 17 Coupling of genetic algorithm with phase-field alloy deposition model[125]. Copyright Elsevier, 2022.

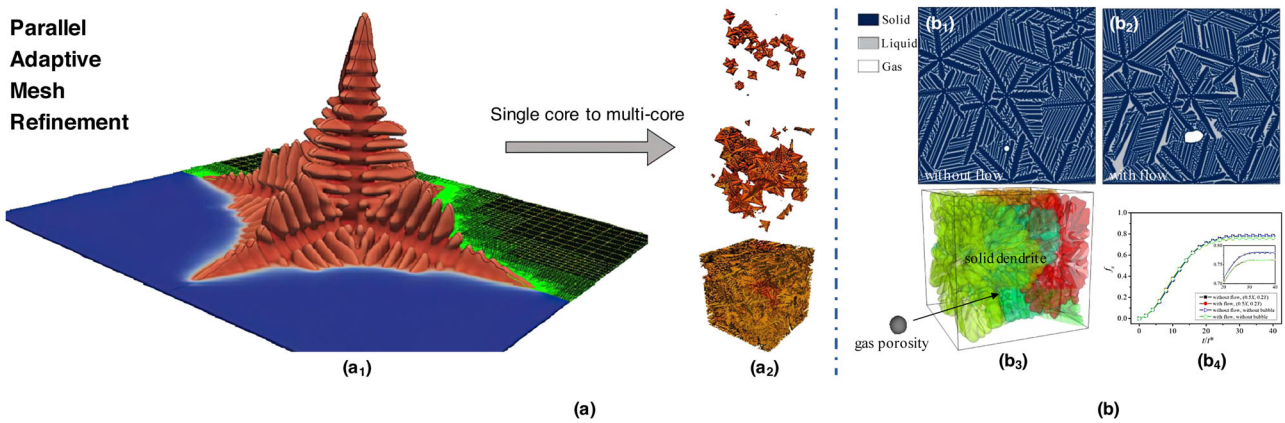

Fig. 18 Dendrites simulation by PFM with AMR. (**a**$_1$) Single dendrite, and (**a**$_2$) polycrystalline dendritic growth[126], from top to bottom, correspond to 6.4 ms (916 K), 12.8 ms (913 K), and 19.1 ms (910 K), respectively. Copyright Elsevier, 2021. **b** Gas porosity[128] in ten dendrites and hydrogen bubbles without flow (**b**$_1$) and with flow (**b**$_2$) in 2D, (**b**$_3$) five dendrites and hydrogen bubbles in 3D; (**b**$_4$) Solid fraction versus time. Copyright Elsevier, 2017.

population, fitness computation, selection, crossover, and mutation, etc. In recent computational studies, Sugathan et al.[124] introduced the effective Landau coefficients that are optimized by genetic algorithms to phase-field free energy equations for ferroelectric switching characteristics. The simulation results showed introducing a lower ferroelectric phase fraction, more crystal structure, and more columnar grain was preferable for ferroelectric applications.

Desai et al.[125] discovered novel, time-dependent protocols with time-varying deposition rate and mobility using genetic algorithm. Coupling with PFM, the targeted microstructures can be obtained, such as the lateral concentration modulation with lower deposition rate and higher deposition time, the vertical concentration modulation with high deposition rate, and hierarchical concentration modulation falling in the middle, the workflow is shown in Fig. 17.

Advanced numerical schemes for high calculation efficiency

PFM is relatively slow to explore large composition-processing-microstructure-properties space. In addition to the above machine learning methods, the phase-field community has also been exploring a variety of novel algorithmic solutions to speed up and accelerate phase-field simulations.

Adaptive mesh refinement. Adaptive mesh refinement (AMR) is an effective tool for numerically solving partial differential equations in arbitrarily shaped and complex regions. By automatically changing the mesh size according to specific needs of different regions[126], the number of meshes is reduced to save computing time. Besides, AMR is often used to extend the simulation length equivalent to actual experimental scale, without disturbing resolution on thin interfaces. For instance, the PF models of solidification and fracture are typical representatives, but with some difficulties in implementation and programming.

When AMR is used for dendrite growth during solidification, especially with thermal diffusion[127], gas porosity[128], melt convection[129], the fine meshes are dynamically employed in interface region, while coarse meshes are in elsewhere. Figure 18 gives two examples of dendritic growth simulated by PFM with AMR.

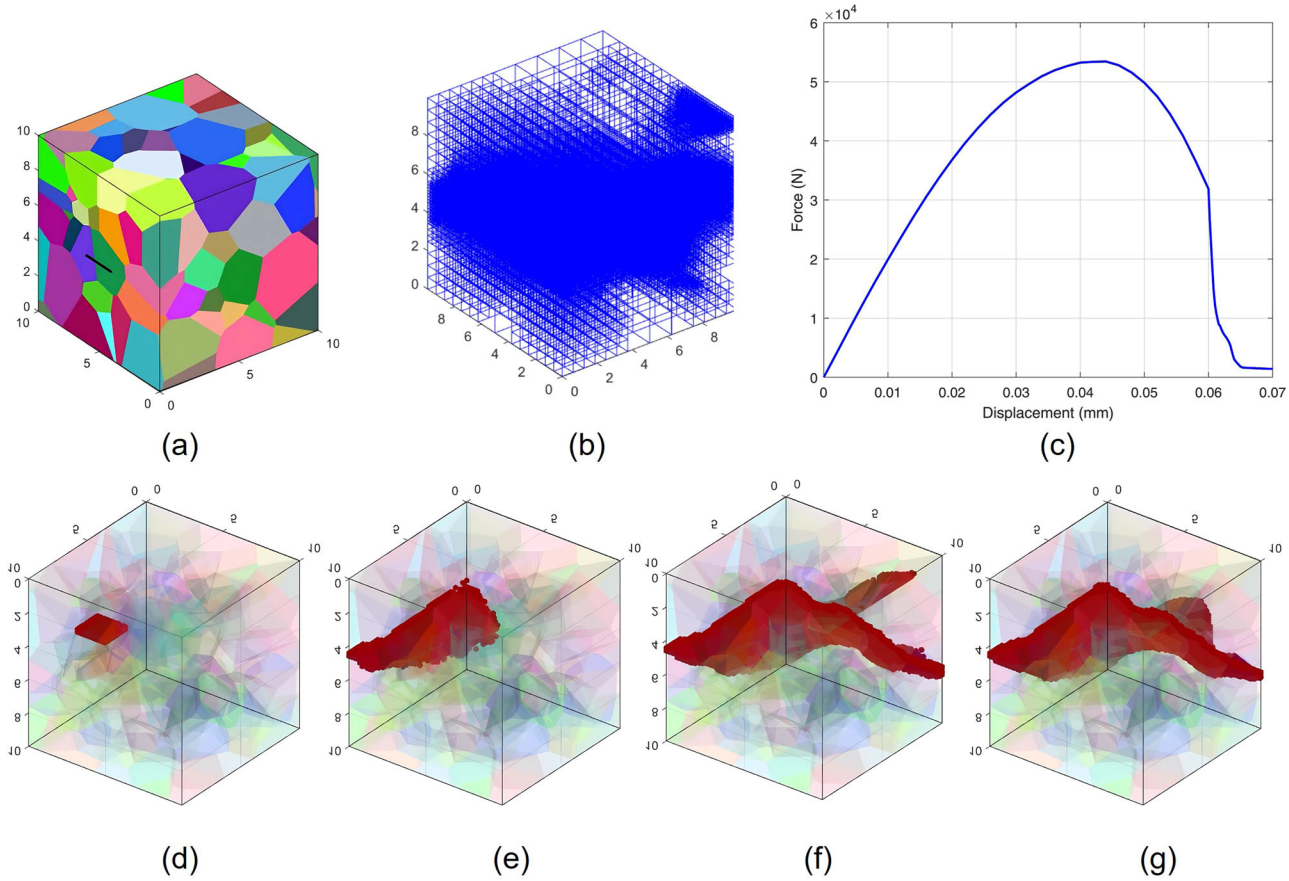

Fig. 19 Crack propagation in a 3D polycrystalline structure[131]. **a** 3D polycrystalline structure with 150 grains. **b** Adaptive mesh refinement at displacement step $u = 7.0\times10^{-3}$ mm. **c** The force–displacement curve. The crack surfaces at different propagation stages: **d** $u = 4.0\times10^{-3}$ mm, **e** $u = 6.2\times10^{-3}$ mm, **f** $u = 6.6\times10^{-3}$ mm, and **g** $u = 7.0\times10^{-3}$mm. Copyright Elsevier, 2020.

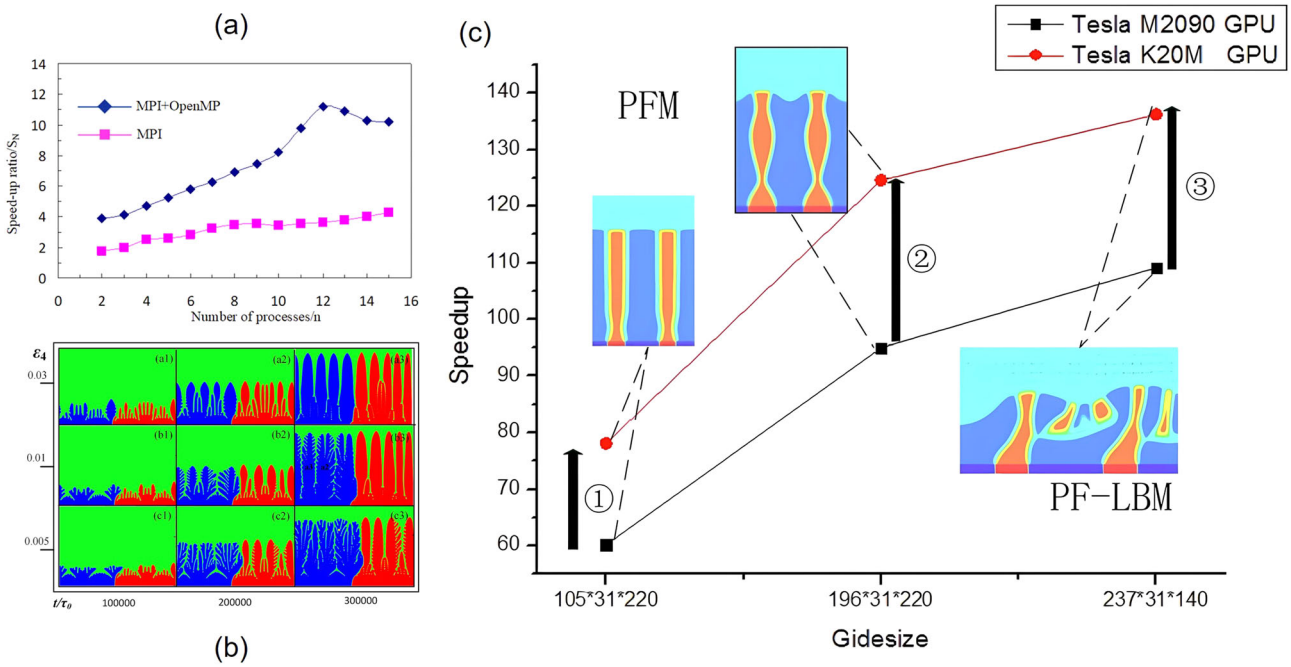

Fig. 20 Typical cases of phase-field simulation with heterogeneous parallel platform for high performance computing. a, **b** Dendrite groeth[144] (Figure adapted with permission from ref. [144], CC BY 4.0.) and **c** Morphology of eutectic with and without fluid flow[141]. Copyright Elsevier, 2020.

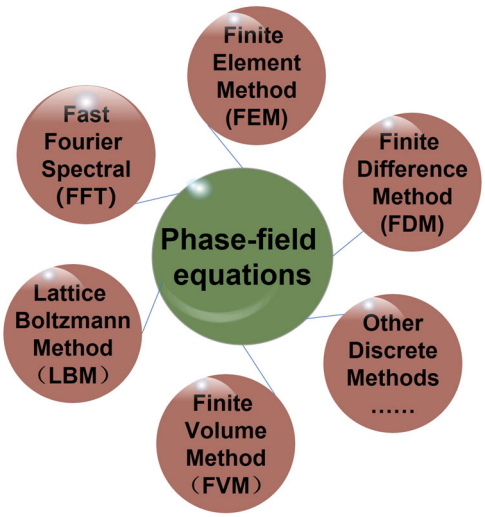

Fig. 21 Typical numerical discrete methods of PF equations. For example, FEM, FDM, FFT, LBM, FVM, etc.

Compared with the uniform mesh, the calculation efficiency is improved by 1-2 orders of magnitude[126].

Generally, the mesh unit size near crack tip needs to be less than half of the length scale in phase-field fracture model. AMR-PF strategy has been used to simulate crack initiation and propagation[130,131], brittle fracture[132,133], ductile fracture[134], etc. An example of AMR-PF simulation of crack propagation in polycrystals is shown in Fig. 19, and the computational time is 2.2 times faster than that known[135].

GPU technique. The parallel GPU (Graphics Processing Unit) is a popular tool for large-scale and high-performance computing owing to the massive computation and high memory bandwidth[136]. Computation with GPU is about 36 times faster than that with a single Central Processing Unit (CPU) core[137].

The heterogeneous parallel platform, composed of different architectures such as Compute Unified Device Architecture (CUDA), Open Computing Language (OpenCL), and combined with parallel programming methods such as MPI-Message Passing Interface or OpenMP- Open Multi Processing, is an effective means for overcoming the shortcomings of large amount of calculation, small simulation scale, and usually limited to qualitative research. For example, GPU+CUDA or MPI+CUDA+GPU for calculating 3D

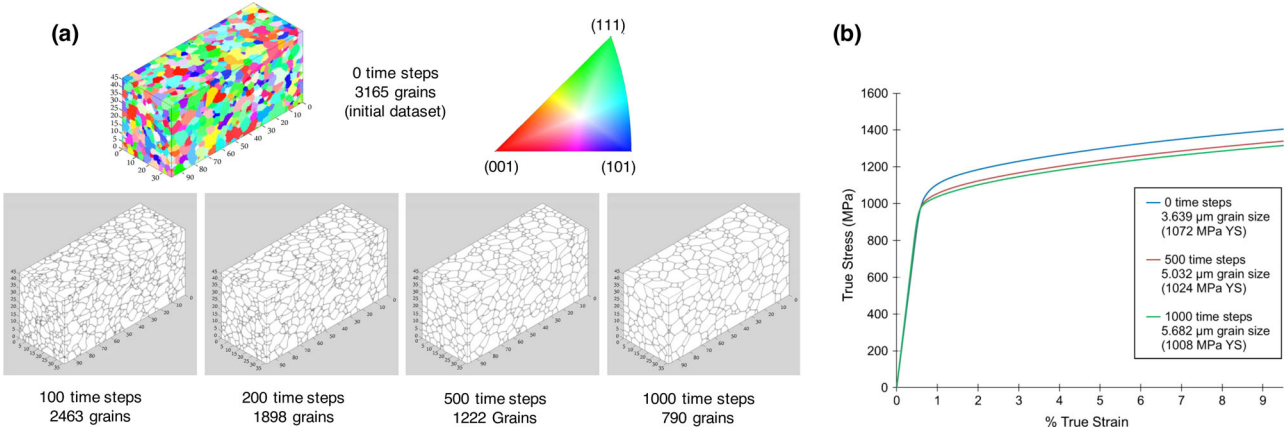

Fig. 22 Outline of the process-structure-performance relationship[145]. a Output from the grain growth by PFM at timestep 0, 100, 200, 500, and 1000 in IN100 alloy, the grains number reduced from 3165 to 790 over 1000 timesteps. **b** Simulated stress-strain response for 0, 500 and 1000 timesteps, representing grain size effects. Copyright Elsevier, 2012.

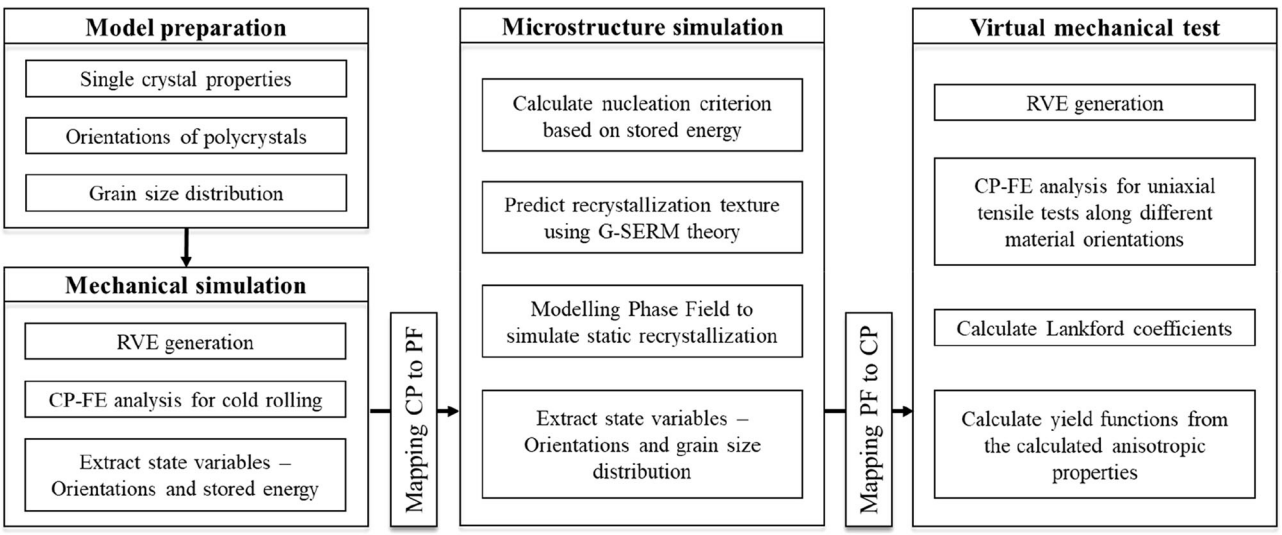

Fig. 23 Flow chart of the integrated CPFE-PF approach[146]. Copyright Elsevier, 2020.

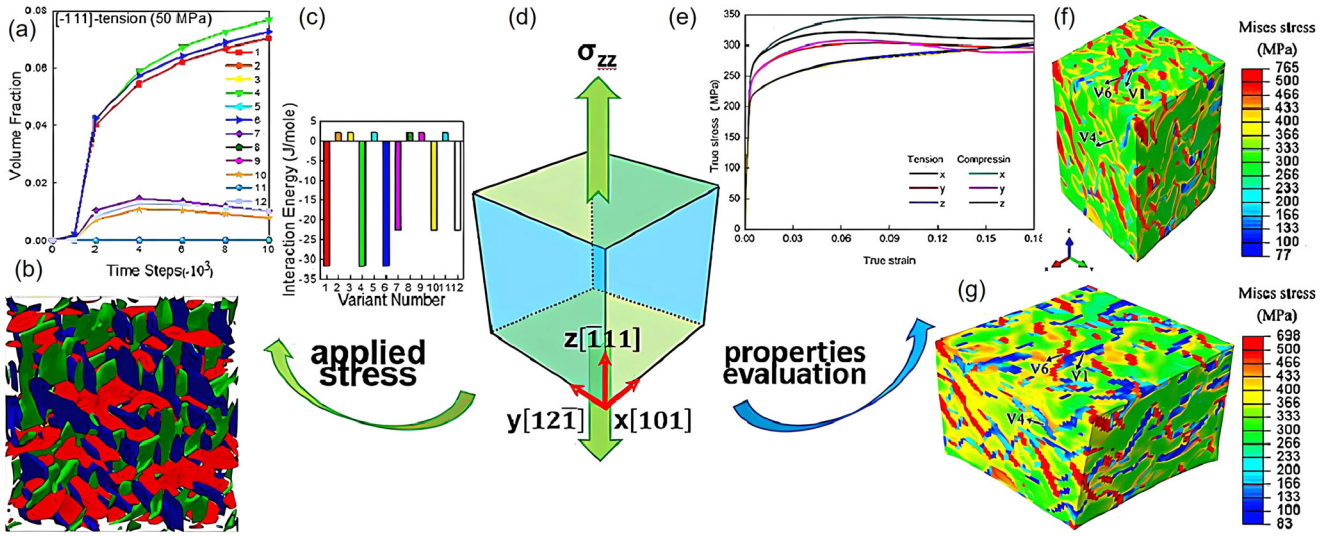

Fig. 24 A complete closed loop from microstructure prediction by PFM to mechanical performance evaluation by CPFEM[147]. **a** Volume fraction of each variant with tension stresses of 50 MPa along $[-111]_{\beta}$. **b** The cross-section of the variant cluster. **c** Elastic interaction energy of 50 MPa tension stress along $[-111]_{\beta}$. **d** Schematic of applied stress. **e** True stress-strain curves. **f**, **g** Mises stress distribution after 20% tension and compression. Copyright Elsevier, 2020.

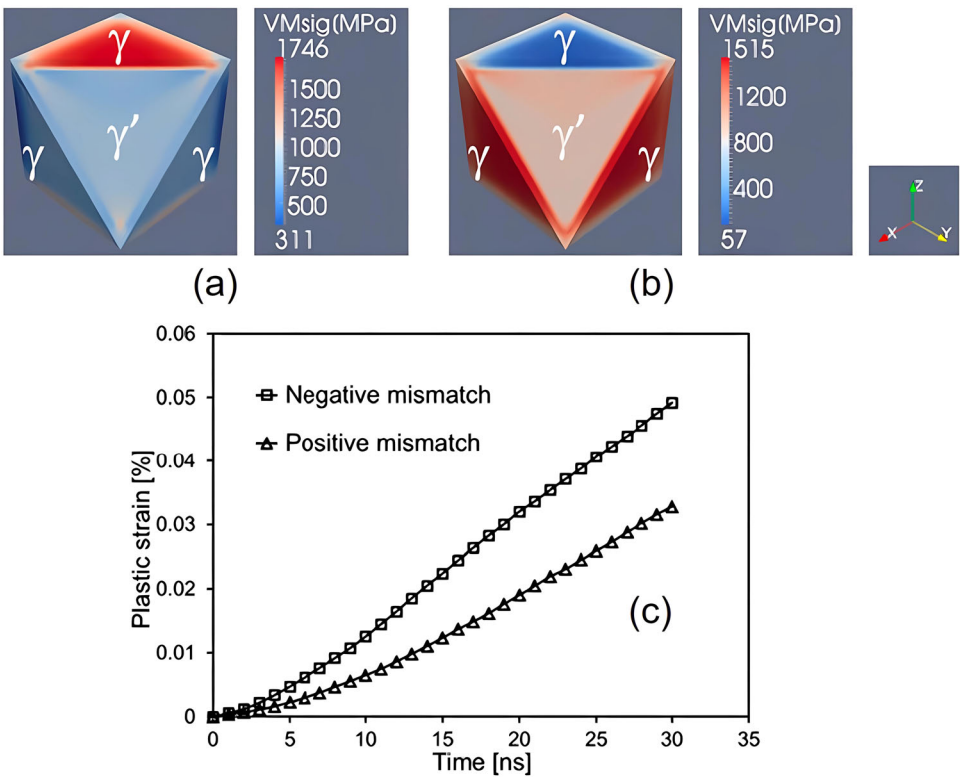

Fig. 25 Effect of mismatch strain on creep behavior[150]. The internal misfit stresses for (**a**) negative mismatch $\delta = -0.005$ and (**b**) positive mismatch $\delta = 0.005$. **c** Plastic strains change with simulation time. Copyright Elsevier, 2018.

dendritic growth[138,139], OpenCL + GPU for eutectic growth[140,141] and eutectoid growth[142], MPI + OpenCL +GPU for dendrite growth[143], MPI +OpenMP for algal and dendritic growth[144].

Figure 20 lists two examples using a heterogeneous parallel platform. MPI +OpenMP hybrid parallel programming is faster than that using only MPI parallel method to simulate dendrite growth, as shown in Fig. 20a, b. Compared with CPU serial program, the computational efficiency for simulating eutectic growth based on GPU has increased by two orders of magnitude, as shown in Fig. 20c. However, the calculation time of small-scale simulation may be longer, because it takes extra time to create and release parallel domains and data transmission.

So, traditional accelerated algorithms (AMR, GPU, etc.), and machine learning technologies (RNN, CNN-LSTM, DeepONet, etc.) are all necessary for accelerating phase-field simulation to design high-performance alloys.

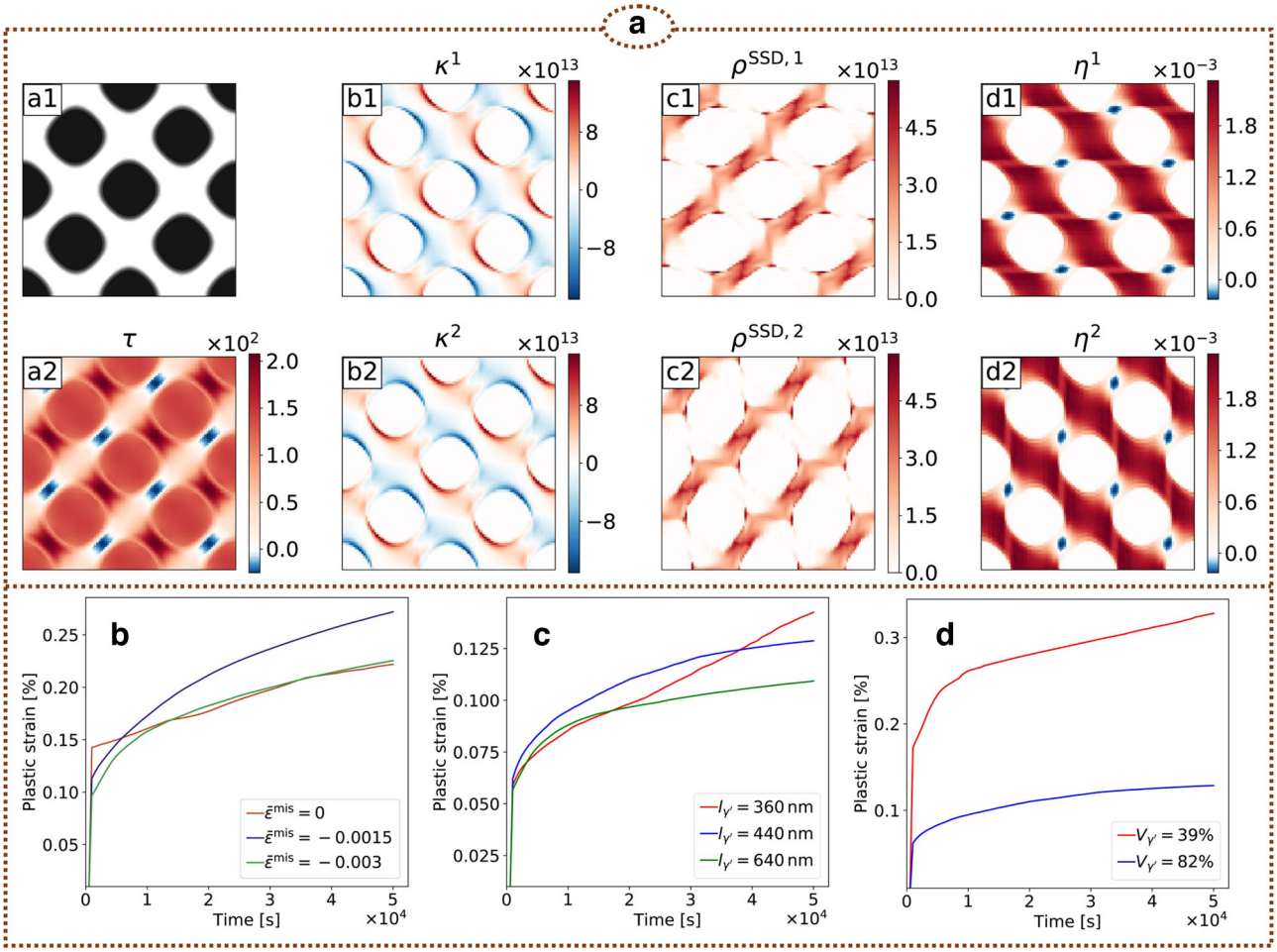

Fig. 26 The creep behavior of single crystal Nickel-based superalloys[153]. a Microstructure of $\bar{\varepsilon}^{mis} = -0.003$ at the first PF time step, (**a**$_1$) γ/γ′ microstructure, (**a**$_2$) long range stress, (**b**$_1$, **b**$_2$) excess dislocation density in slip system 1 and 2, (**c**$_1$, **c**$_2$) statistical stored dislocation density in slip system 1 and 2, (**d**$_1$, **d**$_2$) plastic slip in slip system 1 and 2. Plastic strain with (**b**) different γ/γ′ misfits, (**c**) γ′ edge length, and (**d**) γ′ volume fractions. Copyright Elsevier, 2018.

Coupling with discrete models of continuum system

Using numerical discrete models of macro or micro continuum materials, including finite element model (FEM), finite difference model (FDM), finite volume model (FVM) and fast Fourier transformation (FFT) spectral method, etc, to connect the microstructure characteristics of micro areas with mechanical properties of the same macro continuum through thermodynamic parameters, is a promising approach for "virtual machining" and "virtual design" of novel metallic materials. It should be pointed out that in some published literature, FEM is unilaterally defined as a physical modeling method applicable to macro systems, which is not appropriate, because FEM is really a numerical discrete technique for continuum media consisting of elements with no physical meaning. Only when coupled with various constitutive or physical equations can it have corresponding physical definitions. As shown in Fig. 21, like FDM, FEM can be used to discretize and solve the phase-field equations on micro scale, that is, the micro phase-field equations can be numerically solved by FEM, FDM, FVM, LBM or FFT, etc. Hence, FEM is really a discrete method, which can be used in any continuum system on any spatial scale, including micro and macro scales.

The grain size is often used to bridge the PFM describing process-microstructure relation and the crystal plasticity (CP) FE model describing microstructure-property relation, and a process-structure-performance relationship is built[145], as shown in Fig. 22. The grain growth process and grain size distribution of IN100 alloy annealed at 650 °C obtained from PF simulation are input into the CPFE model to analyze the influence of precipitate size and volume fraction with different annealing time on mechanical properties of the alloy.

Min et al.[146] developed a CPFE model coupled phase-field (CPFE-PF) model to predict the relationship among thermo-mechanical process, microstructure evolution, and mechanical properties of ultra-low carbon steel, the flow chart is shown in Fig. 23. The state variables including grain size, orientation and stored energy are transferred between the models, then the CPFE-PF model for rolling deformation of ultra-low carbon steel was verified experimentally, showing that the computing model was consistent with the experiment when appropriate number of grains were contained.

Using a similar CPFE-PF framework, a closed loop from microstructure prediction to corresponding mechanical performance evaluation of $\alpha + \beta$ titanium alloys was established[147] (Fig. 24). PFM was used to investigate the variant selection of α precipitate in Ti-6Al-4V alloy under specifically applied stresses, and the mechanical properties of typical microstructures under fatigue stress, normal stress, and shear stress were evaluated by using CPFE model. It was found that the micro-texture formed under shear deformation brings the alloy higher strength.

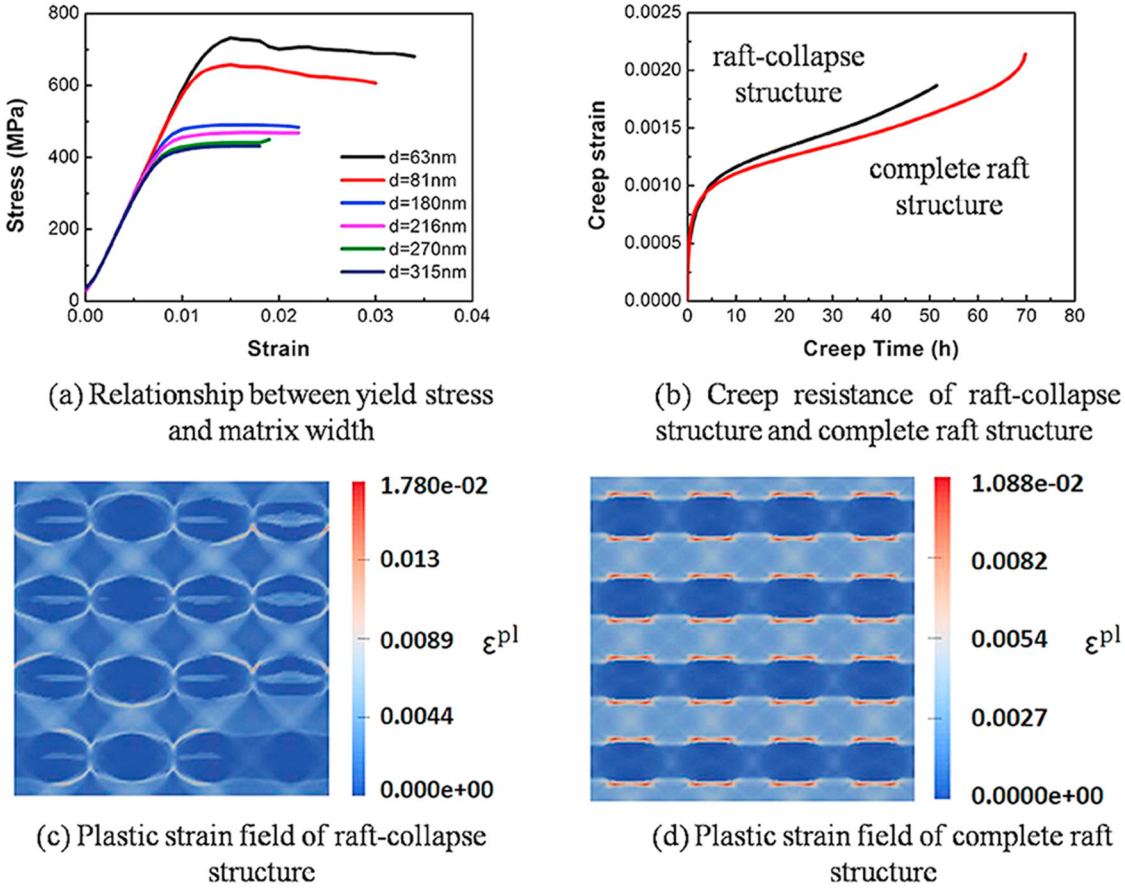

Fig. 27 The yield characteristics and creep resistance of Ni-based superalloys simulated by PFM[158]. **a** Simulation of tensile for γ′/γ microstructure with different matrix channel widths. **b** Simulation of creep with one γ′ variant. **c**, **d** Plastic strain fields from PF simulation. Copyright Elsevier, 2018.

Integrating constitutive relations

In fact, in previous sections of this review, when elastic strain energy or plastic deformation energy is added to the free energy in Cahn-Hillard equation or Alen-Cahn equation, or when PFM is combined with crystal plasticity (CP) theory, PFM already has been coupled with constitutive equation of the material. So, here we just list several common constitutive equations combined with PF model, including elastic (E), elastic-plastic (EP), visco-plastic (VP), rigid-plastic (RP), visco-elastic (VE), and elastic visco-plastic (EVP) models, see Supplementary Note II for details.

The EP-dislocation dynamics models (DDM) include discrete dislocation dynamics (DDD) for dislocation line[148] and continuous dislocation dynamics (CDD) for dislocation density. Gao et al. used DDD to discuss the relation between creep properties and microstructure, including volume fraction[149], morphology resulting from misfit stresses[150], and crystallographic orientation[151] of γ′ phase, and found that the best deformation performance was due to narrow and homogeneous γ matrix channels, and small positive lattice mismatch between γ and γ′ phase as shown in Fig. 25. However, this model is limited to the dislocation motion in static precipitates.

To describe the co-evolution of both precipitate and dislocation during the whole creep stage, Wu et al. used the coupling method of EP-CDD and PFM in single crystal superalloys[152–154]. They found that in the initial creep stage, the primary γ/γ′ microstructure, i.e., smaller γ/γ′ misfit, larger γ′ size, and higher γ′ volume fraction, can result in better creep resistance[3], as shown in Fig. 26. Furthermore, another coupling model of PF and CDD based on plasticity and damage is also established to solve the "swallow-gap" problem in early creep stage and the "dislocation not cutting" problem at tertiary creep stage[154], showing that the increase of dislocation and creep strain in the early and third creep stages are due to the multiplication of dislocation in γ channels and the dislocation cutting into γ′ precipitates respectively.

The visco-plasticity (VP) constitutive relation was added into PFM to study the mechanical properties, rafting behavior[155] and the whole creep stage[156,157] of Ni-based superalloys. Yu et al.[158] developed VP-PF model based on classical flow theory, crystal plasticity, and creep theory to reveal the yield characteristics, rafting behavior, and creep resistance, as shown in Fig. 27. They found that the yield stress was inversely proportional to the width of γ matrix channel resulting from the active slip system shearing into γ′ precipitates, and stable raft structures could improve the creep resistance of superalloys.

Also combining CP analysis and PFM, Liu et al.[159] developed EVP-PF model to investigate the process-structure-property relationship of Ti-6Al-4V alloy in additive manufacturing process, Fig. 28 illustrated some directly relative parameters or variables required to be transferred between different models, showing that equiaxed β-grains and fine α-lath microstructure contribute to high tensile strength.

Optimizing process parameters for high-performance

The optimum composition and processing schedule for the best mechanical properties of alloys can be designed by selecting key factors as evaluation indicators and combining microstructure information obtained from PF simulation and experiment.

Rahnama et al.[160] proposed that the strength change of Fe-15Mn-10Al-0.8C-5Ni and Fe-15Mn-10Al-0.8C (wt.%) light steels

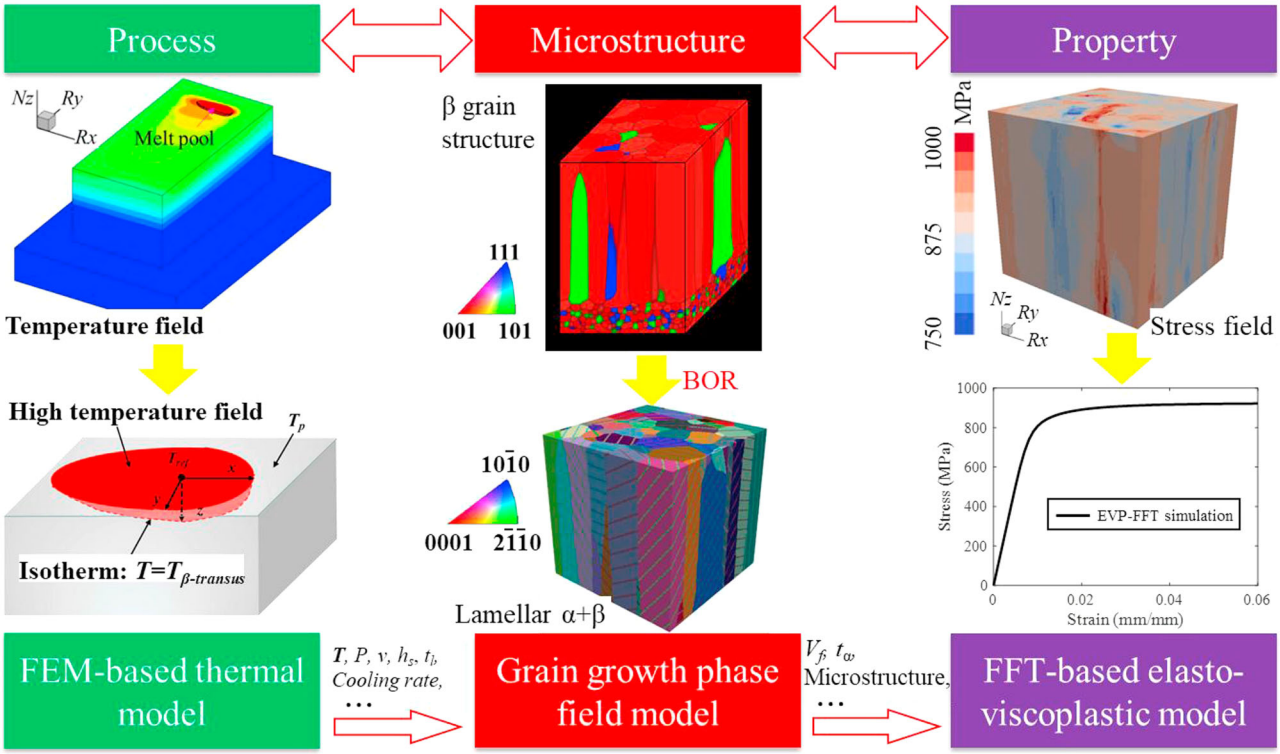

Fig. 28 Schematic of the proposed computational framework to investigate the process-microstructure-property relationship of additive manufacturing- fabricated metallic material[159]. Some directly relative parameters/variables that are required to be transferred between different models are listed, including high-temperature field T, beam power P, scanning speed v, hatching space h_s, layer thickness t_l, cooling rate, the volume fraction of α-phase V_f, α-lath thickness t_α and lamellar $\alpha+\beta$ microstructure and so on. Copyright Elsevier, 2020.

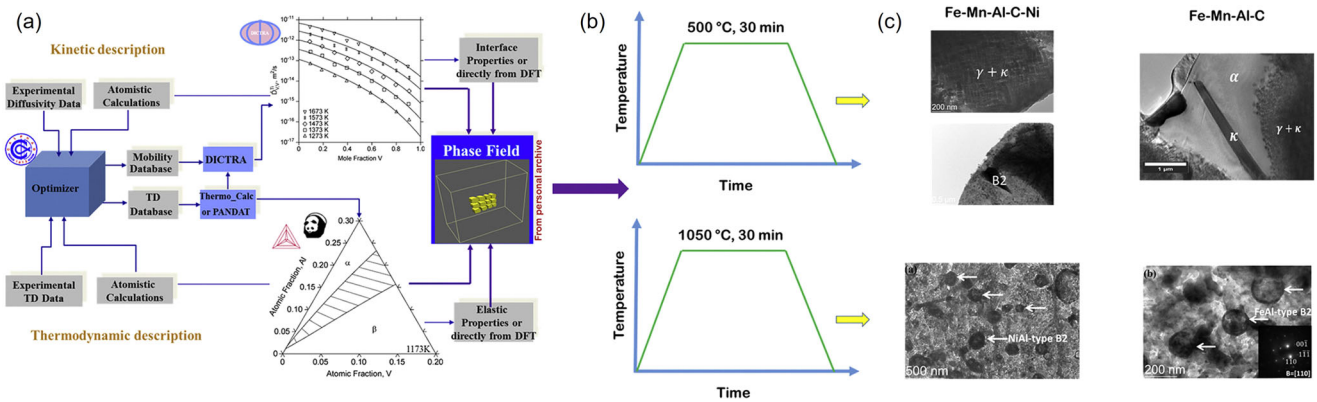

Fig. 29 Design idea in ref. [160]. a PFM coupled with thermodynamics and dynamics. **b** Heat treatment process. **c** The ordered phase morphology. Copyright Elsevier, 2017.

is closely related to the annealing temperature and the morphology of ordered phases. As shown in Fig. 29, the morphology of B2 intermetallics in Fe-Al and Fe-Al-Ni systems and the morphology of κ-carbides in Fe-Mn-Al-C system at different annealing temperatures (500 °C, 700 °C, 900 °C, 1050 °C) were simulated by PFM, it was found that the addition of Ni led to the ordering of α phase and the transformation to a stringer B2 precipitate, preventing the formation of $\alpha+\kappa$ lamellar structure. At 500 °C and 700 °C, the mechanical properties of the alloy were not improved. When annealed at 900 °C and 1050 °C, B2 precipitates changed from faceted shape to disk-like shape, and due to the Ni-Al bond being much stronger than the Fe-Al bond, the alloy shows higher strength (~980 MPa) and lower plasticity (~10%).

Another example, combined with the microstructure simulated by PFM and the sensitivity analysis of actual process parameters, an optimized forging processing window with fine grains was obtained in AZ80 alloy[161–163], which can be applied to guide the multi-step variable speed process in isothermal forging, as shown in Fig. 30, they produced AZ80 alloy parts of high rib and thin web with an average grain size of 9 μm and a grain refinement degree of 77.5%, the maximum yield strength and tensile strength are 268 MPa and 342 MPa respectively.

Geng et al.[164–167] combined the macro CFD model of heat transfer and fluid flow with the micro-PFM for polycrystalline alloy solidification, to investigate the grain/sub-grain evolution during laser welding solidification of 5083 Al sheets, as shown in Fig. 31. Their PF simulation includes two contributions. (i) Select

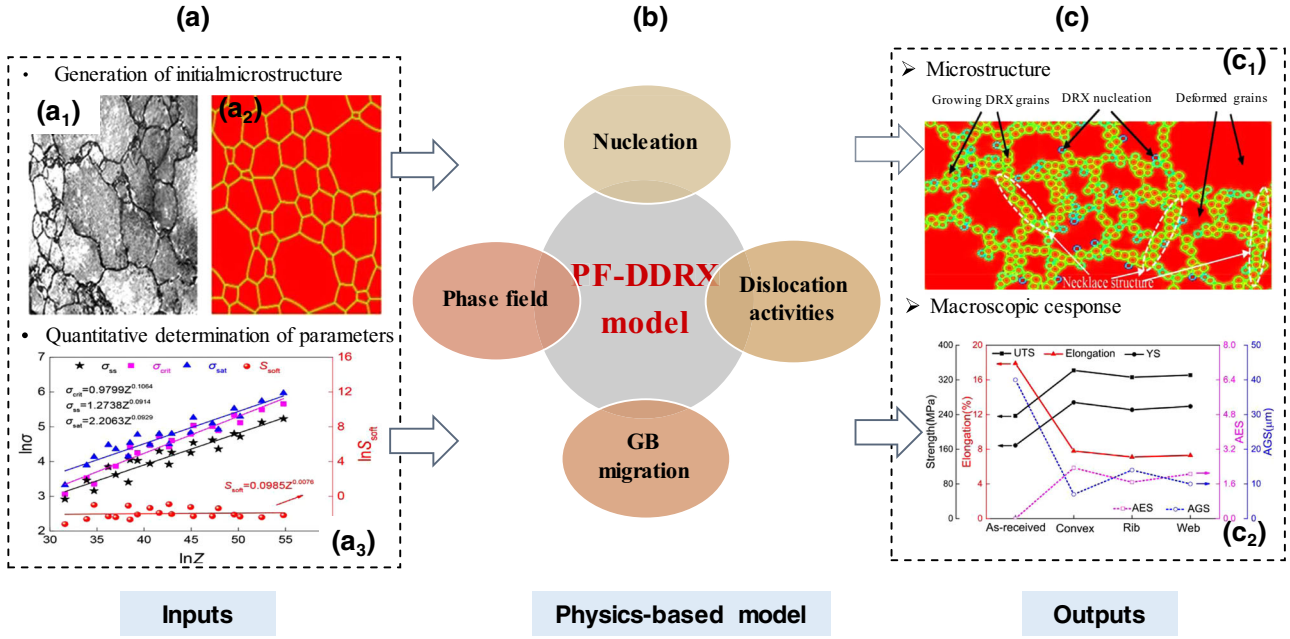

Fig. 30 PF simulation helps optimize forging process[161,163]. ($\mathbf{a_1}$) and ($\mathbf{a_2}$) The grain microstructures obtained from experiments and PF modeling for discontinuous dynamic recrystallization (DDRX), ($\mathbf{a_3}$) Linear relationship between stresses ln σ and lnZ, (**b**) PF-DDRX model framework, ($\mathbf{c_1}$) Predicted grain microstructures at different strains, and ($\mathbf{c_2}$) Mechanical performance response. Copyright Elsevier, 2020.

reasonable welding process parameters. High power matching high welding speed (power should not exceed 3000 W, speed should not exceed 120 mm/s) can reduce columnar crystals and refine dendrite structure. (ii) Increasing nucleation density can significantly refine grains in heterogeneous nucleation. Adding an appropriate amount of Ti (~1.7 wt.%) to the weld can reduce the width of columnar crystal zone and secondary dendrite spacing. The tensile strength of the joint with the above two optimization methods was increased from 303 MPa to 313 MPa and 320 MPa, respectively[167].

CONCLUSION REMARKS AND PROSPECTS

The versatility and easy implementation of PFM make it play an increasingly central role in finding and designing innovative metallic materials, this short review focuses on deciphering the core ideas and some typical applications of PFM in guiding the design of high-performance alloys. Obviously, its applications are far broader than metallic materials, such as ferroelectric/ferromagnetic materials[168,169], nanometer singular materials (graphene[170], metallic glass[171], liquid crystal[172], and aerogel[173]), biomedical[174], polymer[175] and so on. As a matter of fact, it has been extensively applied to predict the microstructure and performance of almost all existing material processes, including melting and solidification, casting, aging, heat treatment, solid phase transformation, forging, welding, creep, deformation, defect evolution, corrosion, irradiation, additive manufacturing, sintering, and fracture failure, etc.

The design strategy of innovative materials with outstanding performance through PF simulation can be roughly divided into three stages. The first stage is to achieve cross-validation of PF simulation and experiment by comparing microstructure morphology. The second stage is to introduce the relationship between microstructure and macro performance into PFM. The third stage is to optimize the process parameters, screen out the best microstructure, and ultimately guide the design of high-performance alloy through PFM integrated with various computing and experimental and machine learning methods. At any stage, the goal of integrated PFM simulation is to design high-performance materials and optimize their manufacturing processes accurately, efficiently, energy-saving and economically.

To this end, several upgrading strategies are proposed here, but not limited to these, to achieve the perfect cohesion and implementation of the above different stages and ultimate goals.

- It is necessary to establish a multi-level unified PFM, which takes the conserved or non-conserved field variables with multiple physical meanings as the multiscale order parameters, combines thermodynamic conditions, dynamic processes and free energy function modeling theory, and can fully consider various internal and external processes of multicomponent, multiphase and polycrystalline systems.
- Strengthen the integration of multi-scale computing methods and experiments, that is, combine the first principles, molecular dynamics, cellular automata, crystal plasticity theory, flow fluid mechanics, machine learning, experiment, and other methods to transfer multi-directional data, which is helpful to achieve the convert and intersection of materials and process design information at different spatial and temporal scales.
- It is necessary to further establish a variety of fast numerical algorithms and reliable large-scale Message Passing Interface (MPI) parallel computing technologies for PF equations based on FEM, FFT, FVM, FDM, LBM, etc., and it is also urgent to combine various macro process optimization technologies or industrial software packages to accelerate the prediction, design, optimization and production of high-performance alloys and actual components.

FUNDAMENTAL THEORY OF PHASE-FIELD MODEL

The comprehensive reviews of PFM were first published in the *Annual Review of Materials Research* by Chen[176] and Karma[177] in 2002. Since then, many review articles of PFM with different emphasis[36,38,178–181] have emerged.

In PFM, two types of field variables that are continuous across the interface are used to describe the microstructure evolution. Conserved field variables are related to density quantities, such as

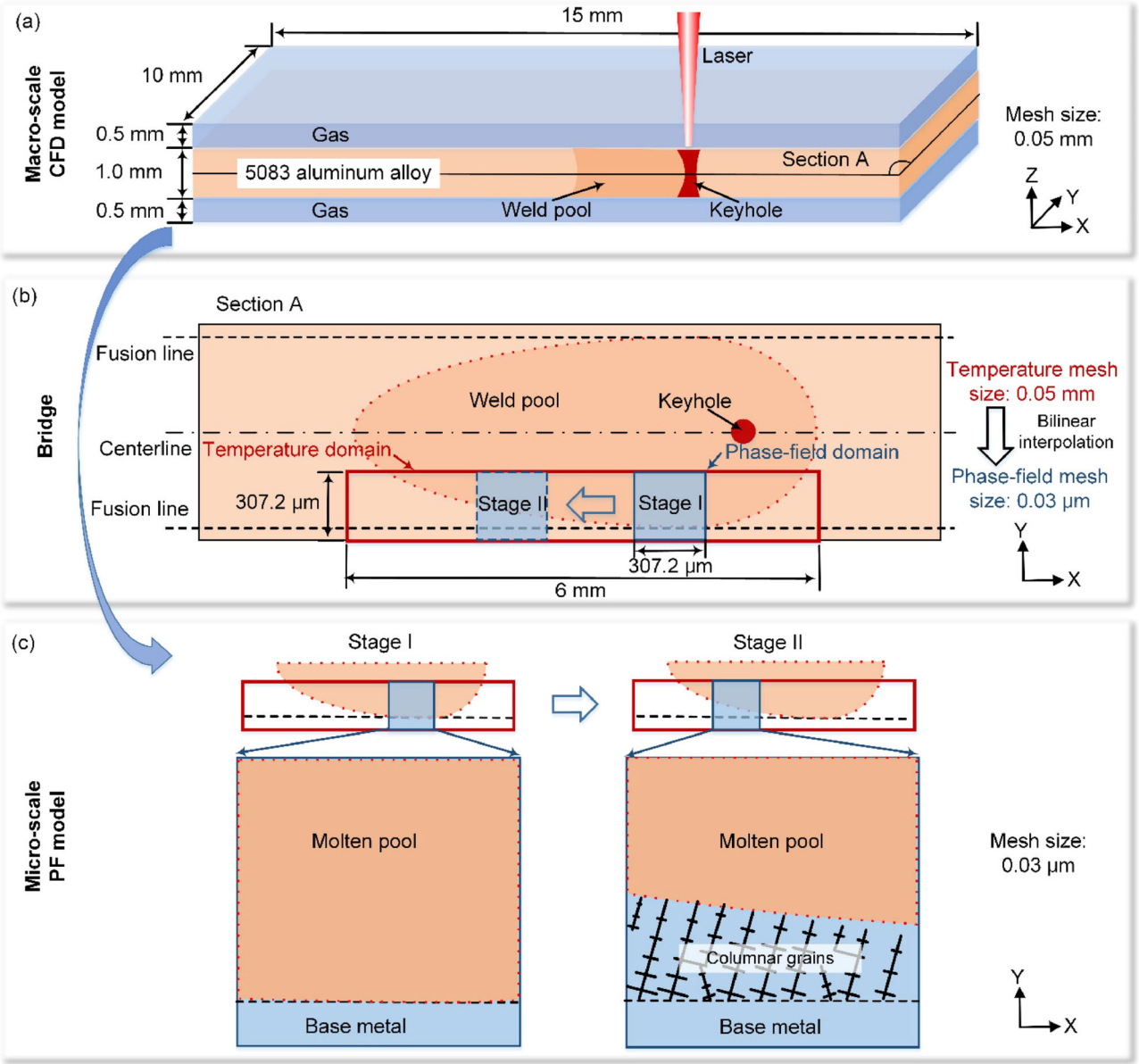

Fig. 31 Schematic of the multi-scale model for simulating grain/sub-grain structure during solidification in the laser molten pool[190]. **a** The macro-scale 3D heat transfer and fluid flow model. **b** The relationship between 3D macro-scale model and 2D micro-scale PF model. **c** The 2D micro-scale PF model. Copyright Elsevier, 2019.

local concentration, atomic occupation probability, or atom average density, etc., the governing equation is given by Cahn-Hilliard equation[182],

$$\frac{\partial c_i(\boldsymbol{r},t)}{\partial t} = \nabla M_{ij} \nabla \frac{\delta F}{\delta c_j(\boldsymbol{r},t)}, i,j = 1,2,\cdots,n \tag{7}$$

where F is the total free energy of the system, $c_1, c_2, \cdots c_n(\boldsymbol{r},t)$ are the conserved field variable which is continuous at spatial coordinate $\boldsymbol{r}$ and time t, ∇ is Hamiltonian operator, M_{ij} is the atomic mobility between components i and j, $\frac{\delta F}{\delta c_j(\boldsymbol{r},t)}$ denotes the thermodynamic driving force.

The evolution of non-conserved field variables related to structural symmetric parameters, such as long-range order parameter, elastic or plastic strain, polarization, structural variant, etc., is controlled by Allen-Cahn equation[183],

$$\frac{\partial \eta_\alpha(\boldsymbol{r},t)}{\partial t} = -L_{\alpha\beta} \frac{\partial F}{\partial \eta_\beta(\boldsymbol{r},t)}, \alpha,\beta = 1,2,\cdots,\mathrm{p} \tag{8}$$

where $\eta_1, \eta_2, \cdots \eta_\mathrm{p}(\boldsymbol{r},t)$ are non-conserved field variables, $L_{\alpha\beta}$ denotes the structural relaxation coefficient, M_{ij} and are $L_{\alpha\beta}$ can be determined by thermodynamic and diffusion kinetic databases[47].

The free energy function generally includes the following,

$$F = \int_\Gamma [f_{\mathrm{loc}} + f_{\mathrm{grad}} + f_{\mathrm{add}}]\mathrm{d}V \tag{9}$$

where the local free energy density f_{loc} is a function of various field variables, i.e., composition c_i, long-range ordered parameters η_i, polarization p_i, magnetization m_i, strain ε_{ij}, etc. The quantitative models for real alloys require careful identification of parameters and constitutive relations from thermodynamic databases, CALPHAD, experiments, or other computational methods.

The gradient energy term describes the energy contribution at interface or domain,

$$f_{\mathrm{grad}} = \sum_j^N \frac{\kappa_j}{2} |\nabla c_i|^2 + \sum_j^M \frac{\kappa_j}{2} |\nabla \eta_j|^2 \tag{10}$$

where κ_i and κ_j are the gradient coefficient, which can affect the interface width and interface energy. N and M are the number of conserved and non-conserved field variables respectively.

f_{add} is additional energy including elastic strain energy, plastic deformation energy, magnetic energy, or electrical energy, etc. The competition between the contributions of these different physical phenomena to the total energy quickly and efficiently outlines the colorful microstructure morphology, making up for the lack of experimental measures that are difficult to dynamically capture information from nano to mesoscopic scales.

Recently, from the perspective of various order parameters, coupling of multi-physical fields and integration with some advanced algorithms or machine learning methods, the integrated phase-field method (IPFM)[184] can be included in the framework of materials genome initiative (MGI) and integrated computational materials engineering (ICME), which is more conductive to better application of phase-field method in more engineering materials design.

DATA AVAILABILITY

Data will be made available on request.

Received: 9 January 2023; Accepted: 9 May 2023;
Published online: 01 June 2023

REFERENCES

1. Tourret, D., Liu, H. & Llorca, J. Phase-field modeling of microstructure evolution: recent applications, perspectives and challenges. *Prog. Mater. Sci.* **123**, 100810 (2022).
2. Ren, J. et al. Strong yet ductile nanolamellar high-entropy alloys by additive manufacturing. *Nature* **608**, 62–68 (2022).
3. Li, H. et al. Uniting tensile ductility with ultrahigh strength via composition undulation. *Nature* **604**, 273–279 (2022).
4. Wang, H. et al. Manufacture-friendly nanostructured metals stabilized by dual-phase honeycomb shell. *Nat. Commun.* **13**, 2034 (2022).
5. Dong, R. F. et al. Correlation between the mechanical properties and the (110) texture in a hot-rolled near beta titanium alloy. *J. Mater. Sci. Technol.* **97**, 165–168 (2022).
6. Fix, G. J. Phase field methods for free boundary problems, in *Free Boundary Problems: Theory and Applications*, (eds, B. Fasano & M. Primicerio) (Pitman, London, 1983).
7. Chen, L. Q. & Khachaturyan, A. G. Computer simulation of structural transformations during precipitation of an ordered intermetallic phase. *Acta Metall. Mater.* **39**, 2533–2551 (1991).
8. Elder, K. R., Katakowski, M., Haataja, M. & Grant, M. Modeling elasticity in crystal growth. *Phys. Rev. Lett.* **88**, 245701 (2002).
9. Zhao, Y. H., Liu, K. X., Hou, H. & Chen, L. Q. Role of interfacial energy anisotropy in dendrite orientation in Al-Zn alloys: A phase field study. *Mater. Des.* **216**, 110555 (2022).
10. Kulkarni, A. A., Hanson, E., Zhang, R., Thornton, K. & Braun, P. V. Archimedean lattices emerge in template-directed eutectic solidification. *Nature* **577**, 355–358 (2020).
11. Choudhury, A., Nestler, B., Telang, A., Selzer, M. & Wendler, F. Growth morphologies in peritectic solidification of Fe–C: A phase-field study. *Acta Mater.* **58**, 3815–3823 (2010).
12. Koyama, T., Hashimoto, K. & Onodera, H. Phase-field simulation of phase transformation in Fe-Cu-Mn-Ni quaternary alloy. *Mater. Trans.* **47**, 2765–2772 (2006).
13. Zhang, L., Xiang, Z. L., Li, X. D. & Wang, E. G. Spinodal decomposition in Fe-25Cr-12Co alloys under the influence of high magnetic field and the effect of grain boundary. *Nanomaterials* **8**, 578 (2018).
14. Chen, L. Q. & Yang, W. Computer simulation of the domain dynamics of a quenched system with a large number of nonconserved order parameters: The grain-growth kinetics. *Phys. Rev. B* **50**, 15752–15756 (1994).
15. Ahmed, H., Sreekar, R., Grethe, W. & Anter, E.-A. Impact of the plastic deformation microstructure in metals on the kinetics of recrystallization: A phase-field study. *Acta Mater.* **240**, 118332 (2022).
16. Rajasekhara, S. & Ferreira, P. J. Martensite→austenite phase transformation kinetics in an ultrafine-grained metastable austenitic stainless steel. *Acta Mater.* **59**, 738–748 (2011).
17. Aranas, C. Jr, Rodrigues, S., Siciliano, F. & Jonas, J. In-situ X-ray diffraction evidence of dynamic transformation of austenite to ferrite during hot compression test in the single austenite phase field. *Scr. Mater.* **177**, 86–90 (2020).
18. Mushongera, L. T., Amos, P. K., Schoof, E., Kumar, P. & Nestler, B. The non-steady-state growth of divergent pearlite in Fe-C-Mn steels: a phase-field investigation. *J. Mater. Sci.* **55**, 5280–5295 (2020).
19. Toloui, M. & Militzer, M. Phase field modeling of the simultaneous formation of bainite and ferrite in TRIP steel. *Acta Mater.* **144**, 786–800 (2018).
20. Wang, Y. Z. & Khachaturyan, A. G. Multi-scale phase field approach to martensitic transformations. *Mat. Sci. Eng. A.* **438**, 55–63 (2006).
21. Wang, Y. Y., Ding, J. H., Chen, Y. G., Zhao, J. J. & Wang, Y. Z. Three-dimensional phase field simulation of intragranular void formation and thermal conductivity in irradiated alpha-Fe. *J. Mater. Sci.* **53**, 11002–11014 (2018).
22. Zhao, Y. H. et al. Dislocation motion in plastic deformation of nano polycrystalline metal materials: a phase field crystal method study. *Adv. Compos. Hybrid. Mater.* **5**, 2546–2556 (2022).
23. Tian, X. L. et al. Phase-field crystal simulation of evolution of liquid pools in grain boundary pre-melting regions. *T. Nonfer. Metal. Soc.* **31**, 1175–1188 (2021).
24. Clayton, J. D. & Knap, J. Phase-field analysis of fracture-induced twinning in single crystals. *Acta Mater.* **61**, 5341–5353 (2013).
25. Karma, A. Phase-field formulation for quantitative modeling of alloy solidification. *Phys. Rev. Lett.* **87**, 115701 (2001).
26. Echebarria, B. Quantitative phase-field model for alloy solidification. *Phys. Rev. E.* **70**, 061604 (2004).
27. Zhao, Y. H., Zhang, B., Hou, H., Chen, W. P. & Wang, M. Phase-field simulation for the evolution of solid/liquid interface front in directional solidification process. *J. Mater. Sci. Technol.* **35**, 1044–1052 (2019).
28. Chen, W. P., Zhao, Y. H., Yang, S., Zhang, D. & Hou, H. Three-dimensional phase-field simulations of the influence of diffusion interface width on dendritic growth of Fe-0.5 wt.%C alloy. *Adv. Compos. Hybrid. Mater.* **4**, 371–378 (2021).
29. Shen, C., Chen, Q., Wen, Y. H., Simmons, J. P. & Wang, Y. Increasing length scale of quantitative phase field modeling of growth-dominant or coarsening-dominant process. *Scr. Mater.* **50**, 1023–1028 (2004).
30. Sun, Y. Y. et al. Multi-component phase-field simulation of microstructural evolution and elemental distribution in Fe-Cu-Mn-Ni-Al alloy. *Calphad* **69**, 101759 (2020).
31. Wu, K. S., Chang, Y. A. & Wang, Y. Z. Simulating interdiffusion microstructures in Ni-Al-Cr diffusion couples: a phase field approach coupled with CALPHAD database. *Scr. Mater.* **50**, 1145–1150 (2004).
32. Zhao, Y. H., Sun, Y. Y. & Hou, H. Core-shell structure nanoprecipitates in Fe-xCu-3.0Mn-1.5Ni-1.5Al alloys: A phase field study. *Prog. Nat. Sci.* **32**, 358–368 (2022).
33. Fallah, V., Stolle, J., Ofori-Opoku, N., Esmaeili, S. & Provatas, N. Phase-field crystal modeling of early stage clustering and precipitation in metal alloys. *Phys. Rev. B* **86**, 134112 (2012).
34. Fallah, V., Korinek, A., Ofori-Opoku, N., Provatas, N. & Esmaeili, S. Atomistic investigation of clustering phenomenon in the Al-Cu system: three-dimensional phase-field crystal simulation and HRTEM/HRSTEM characterization. *Acta Mater.* **61**, 6372–6386 (2013).
35. Fallah, V. et al. Cluster evolution mechanisms during aging in Al-Mg-Si alloys. *Acta Mater.* **103**, 290–300 (2016).
36. Kurz, W., Fisher, D. J. & Trivedi, R. Progress in modelling solidification microstructures in metals and alloys: dendrites and cells from 1700 to 2000. *Int. Mater. Rev.* **64**, 311–354 (2019).
37. Li, J. H., Zhou, X. L., Brochu, M., Provatas, N. & Zhao, Y. F. Solidification microstructure simulation of Ti-6Al-4V in metal additive manufacturing: A review. *Addit. Manuf.* **31**, 100989 (2020).
38. Kurz, W., Rappaz, M. & Trivedi, R. Progress in modelling solidification microstructures in metals and alloys. Part II: dendrites from 2001 to 2018. *Int. Mater. Rev.* **66**, 30–76 (2021).
39. Singer-Loginova, I. & Singer, H. M. The phase field technique for modeling multiphase materials. *Rep. Prog. Phys.* **71**, 106501 (2008).
40. Militzer, M. Phase field modeling of microstructure evolution in steels. *Curr. Opin. Solid State. Mater. Sci.* **15**, 106–115 (2011).
41. Steinbach, I. & Shchyglo, O. Phase-field modelling of microstructure evolution in solids: perspectives and challenges. *Curr. Opin. Solid State. Mater. Sci.* **15**, 87–92 (2011).
42. Bui, T. Q. & Hu, X. F. A review of phase-field models, fundamentals and their applications to composite laminates. *Eng. Fract. Mech.* **248**, 107705 (2021).
43. Zhuang, X., Zhou, S., Huynh, G. D., Aerias, P. & Rabczuk, T. Phase field modelling and computer implementation: A review. *Eng. Fract. Mech.* **262**, 108234 (2022).
44. Ambati, M., Gerasimov, T. & Lorenzis, L. D. A review on phase-field models of brittle fracture and a new fast hybrid formulation. *Comput. Mech.* **55**, 383–405 (2015).
45. Ansari, T. Q., Huang, H. & Shi, S.-Q. Phase field modeling for the morphological and microstructural evolution of metallic materials under environmental attack. *npj Comput. Mater.* **7**, 1–21 (2021).

46. Wang, J.-J., Wang, B. & Chen, L.-Q. Understanding, predicting, and designing ferroelectric domain structures and switching guided by the phase-field method. *Annu. Rev. Mater. Sci.* **49**, 127–152 (2019).
47. Wang, Q. et al. Application of phase-field method in rechargeable batteries. *npj Comput. Mater.* **6**, 176 (2020).
48. Moure, A. & Gomez, H. Phase-field modeling of individual and collective cell migration. *Arch. Comput. Method. Eng.* **28**, 311–334 (2021).
49. Jreidini, P. et al. Orientation gradients in rapidly solidified pure aluminum thin films: comparison of experiments and phase-field crystal simulations. *Phys. Rev. Lett.* **127**, 205701 (2021).
50. Boussinot, G. et al. Laser powder bed fusion of eutectic Al-Ni alloys: Experimental and phase-field studies. *Mater. Des.* **198**, 109299 (2021).
51. Goerler, J. V. et al. Topological phase inversion after long-term thermal exposure of nickel-base superalloys: Experiment and phase-field simulation. *Acta Mater.* **124**, 151–158 (2017).
52. Yang, C., Xu, Q. Y., Su, X. L. & Liu, B. C. Multiphase-field and experimental study of solidification behavior in a nickel-based single crystal superalloy. *Acta Mater.* **175**, 286–296 (2019).
53. Xiao, W. J., Xu, Y. X., Xiao, H., Li, S. M. & Song, L. J. Investigation of the Nb element segregation for laser additive manufacturing of nickel-based superalloys. *Int. J. Heat. Mass Transf.* **180**, 121800 (2021).
54. Li, J. L., Li, Z., Wang, Q., Dong, C. & Liaw, P. K. Phase-field simulation of coherent BCC/B2 microstructures in high entropy alloys. *Acta Mater.* **197**, 10–19 (2020).
55. Yang, G., Song, Y. D., Wang, Q., Zhang, L. B. & Deng, L. J. Review of ionic liquids containing, polymer/inorganic hybrid electrolytes for lithium metal batteries. *Mater. Des.* **190**, 108563 (2020).
56. Liu, Y. et al. Graphene-based interlayer for high-performance lithium-sulfur batteries: A review. *Mater. Des.* **211**, 110171 (2021).
57. Lin, C., Liu, K., Ruan, H. H. & Wang, B. Mechano-electrochemical phase field modeling for formation and modulation of dendritic Pattern: Application to uranium recovery from spent nuclear fuel. *Mater. Des.* **213**, 110322 (2022).
58. Osorio, W. R., Goulart, P. R., Garcia, A., Santos, G. A. & Neto, C. M. Effect of dendritic arm spacing on mechanical properties and corrosion resistance of Al 9 Wt Pct Si and Zn 27 Wt Pct Al alloys. *Metall. Mater. Trans. A* **37**, 2525–2538 (2006).
59. Ferreira, A. F. et al. Investigations on metallurgical parameters in hypoeutectic Al-Si alloys under upward directional solidifications. *Int. J. Adv. Manuf. Technol.* **121**, 7359–7382 (2022).
60. Bellón, B. et al. Multiscale prediction of microstructure length scales in metallic alloy casting. *Acta Mater.* **207**, 116686 (2021).
61. Bai, S., Liu, Z. Y., Zhou, X. W., Gu, Y. X. & Yu, D. E. Strain-induced dissolution of Cu-Mg co-clusters and dynamic recrystallization near a fatigue crack tip of an underaged Al-Cu-Mg alloy during cyclic loading at ambient temperature. *Scri. Mater.* **64**, 1133–1136 (2011).
62. Fallah, V., Ofori-Opoku, N., Stolle, J., Provatas, N. & Esmaeili, S. Simulation of early-stage clustering in ternary metal alloys using the phase-field crystal method. *Acta Mater.* **61**, 3653–3666 (2013).
63. Zhou, X. Y., Kamachali, R. D., Boyce, B. L., Clark, B. G. & Thompson, G. B. Spinodal decomposition in nanocrystalline alloys. *Acta Mater.* **215**, 117054 (2021).
64. Xin, T. Z. et al. Ultrahigh specific strength in a magnesium alloy strengthened by spinodal decomposition. *Sci. Adv.* **7**, ebaf3039 (2021).
65. Xin, T. Z. et al. Phase Transformations in an ultralight BCC Mg alloy during anisothermal aging. *Acta Mater.* **239**, 118248 (2022).
66. Lu, K., Lu, L. & Suresh, S. Strengthening materials by engineering coherent internal boundaries at the nanoscale. *Science* **324**, 349–352 (2009).
67. Ovid'Ko, I. A., Valiev, R. Z. & Zhu, Y. T. Review on superior strength and enhanced ductility of metallic nanomaterials. *Prog. Mater. Sci.* **94**, 462–540 (2018).
68. Zhu, Y. T. et al. Dislocation-twin interactions in nanocrystalline fcc metals. *Acta Mater.* **59**, 812–821 (2011).
69. Kondo, R., Tadano, Y. & Shizawa, K. A phase-field model of twinning and detwinning coupled with dislocation-based crystal plasticity for HCP metals. *Comp. Mater. Sci.* **95**, 672–683 (2014).
70. Ovid'Ko, I. A. & Sheinerman, A. G. Mechanical properties of nanotwinned metals: a review. *Rev. Adv. Mater. Sci.* **44**, 1–25 (2016).
71. Kou, Z. D. et al. Observing dislocations transported by twin boundaries in Al thin film: unusual pathways for dislocation-twin boundary interactions. *Nano Lett.* **22**, 6229–6234 (2022).
72. Kou, Z. D. et al. Revealing the atomic-scale evolution of sessile disconnections on twin boundaries during deformation. *Scr. Mater.* **221**, 114956 (2022).
73. Elder, K. R., Provatas, N., Berry, J., Stefanovic, P. & Grant, M. Phase-field crystal modeling and classical density functional theory of freezing. *Phys. Rev. B* **75**, 064107 (2007).
74. Tian, X. L. et al. Cooperative effect of strength and ductility processed by thermomechanical treatment for Cu-Al-Ni alloy. *Mater. Sci. Eng. A.* **849**, 143485 (2022).
75. Li, Y. L., Hu, S. Y., Sun, X. & Stan, M. A review: applications of the phase field method in predicting microstructure and property evolution of irradiated nuclear materials. *npj Comput. Mater.* **3**, 16 (2017).
76. Hu, S. Y., Casella, A. M., Lavender, C. A., Senor, D. J. & Burkes, D. E. Assessment of effective thermal conductivity in U-Mo metallic fuels with distributed gas bubbles. *J. Nucl. Mater.* **462**, 64–76 (2015).
77. Shchyglo, O., Du, G., Engels, J. K. & Steinbach, I. Phase-field simulation of martensite microstructure in low-carbon steel. *Acta Mater.* **175**, 415–425 (2019).
78. Wang, D. et al. Phase field simulation of martensitic transformation in prestrained nanocomposite shape memory alloys. *Acta Mater.* **164**, 99–109 (2019).
79. Xu, B., Yu, C. & Kang, G. Z. Phase field study on the microscopic mechanism of grain size dependent cyclic degradation of super-elasticity and shape memory effect in nano-polycrystalline NiTi alloys. *Int. J. Plast.* **145**, 103075 (2021).
80. Cissé, C. & Zaeem, M. A. A phase-field model for non-isothermal phase transformation and plasticity in polycrystalline yttria-stabilized tetragonal zirconia. *Acta Mater.* **191**, 111–123 (2020).
81. Mamivand, M., Zaeem, M. A. & El Kadiri, H. Phase field modeling of stress-induced tetragonal-to-monoclinic transformation in zirconia and its effect on transformation toughening. *Acta Mater.* **64**, 208–219 (2014).
82. Seol, D. J., Won, Y. M., Oh, K. H., Shin, Y. C. & Yim, C. H. Mechanical behavior of carbon steels in the temperature range of mushy zone. *ISIJ Int.* **40**, 356–363 (2000).
83. Lee, D. N. & Kim, H. S. Plastic yield behaviour of porous metals. *Powder Met.* **35**, 275–280 (1992).
84. Seol, D. J., Oh, K. H., Cho, J. W., Lee, J.-E. & Yoon, U.-S. Phase-field modelling of the thermo-mechanical properties of carbon steels. *Acta Mater.* **50**, 2259–2268 (2002).
85. Ta, N., Zhang, L. J. & Du, Y. Design of the precipitation process for Ni-Al alloys with optimal mechanical properties: a phase-field study. *Metall. Mater. Trans. A.* **45A**, 1787–1802 (2014).
86. Nie, J. F. Effects of precipitate shape and orientation on dispersion strengthening in magnesium alloys. *Scr. Mater.* **48**, 1009–1015 (2003).
87. Liu, H., Wang, Y. Z. & Nie, J. F. Phase Field Simulation of Orowan Strengthening by Coherent Precipitate Plates in a Mg-Nd Alloy. In *Proceedings of the 3rd World Congress on Integrated Computational Materials Engineering* (ICME 2015), 2015.
88. Ji, Y. Z. et al. Predicting β′ precipitate morphology and evolution in Mg-RE alloys using a combination of first-principles calculations and phase-field modeling. *Acta Mater.* **76**, 259–271 (2014).
89. Sun, Y. Z., Luo, J. & Zhu, J. M. Phase field study of the microstructure evolution and thermomechanical properties of polycrystalline shape memory alloys: Grain size effect and rate effect. *Comput. Mater. Sci.* **145**, 252–262 (2018).
90. Dhote, R. P., Melnik, R. V. N. & Zu, J. Dynamic thermo-mechanical coupling and size effects in finite shape memory alloy nanostructures. *Comput. Mater. Sci.* **63**, 105–117 (2012).
91. Ahluwalia, R., Quek, S. S. & Wu, D. T. Simulation of grain size effects in nanocrystalline shape memory alloys. *J. Appl. Phys.* **117**, 244305 (2015).
92. Mianroodi, J. R., Siboni, N. H. & Raabe, D. Computational discovery of energy-efficient heat treatment for microstructure design using deep reinforcement learning. Preprint at https://arxiv.org/pdf/2209.11259.pdf (2022).
93. Batabyal, A. et al. Gaussian process-based model to optimize additively manufactured powder microstructures from phase field modeling. *ASCE-ASME J. Risk Uncertain. Eng. Syst. Part B: Mech. Eng.* **8**, 011102 (2022).
94. Wu, H. Y. et al. A study of solution cooling rate on gamma' precipitate and hardness of a polycrystalline Ni-based superalloy using a high-throughput methodology. *Mater. Sci. Eng. A.* **739**, 473–479 (2019).
95. Jiang, X., Zhang, R. J., Zhang, C., Yin, H. Q. & Qu, X. H. Fast prediction of the quasi phase equilibrium in phase field model for multicomponent alloys based on machine learning method. *Calphad* **66**, 101644 (2019).
96. Kunwar, A., Coutinho, Y. A., Hektor, J., Ma, H. T. & Moelans, N. Integration of machine learning with phase field method to model the electromigration induced Cu_6Sn_5 IMC growth at anode side Cu/Sn interface. *J. Mater. Sci. Technol.* **59**, 203–219 (2020).
97. Zhu, Y. Q. et al. Linear-superelastic Ti-Nb nanocomposite alloys with ultralow modulus via high-throughput phase-field design and machine learning. *npj Comput. Mater.* **7**, 1–10 (2021).
98. Kunwar, A., Hektor, J., Nomoto, S., Coutinho, Y. A. & Moelans, N. Combining multi-phase field simulation with neural network analysis to unravel thermomigration accelerated growth behavior of Cu_6Sn_5 IMC at cold side Cu–Sn interface. *Int. J. Mech. Sci.* **184**, 105843 (2020).
99. Zapiain, D. M. D., Stewart, J. A. & Dingreville, R. Accelerating phase-field-based microstructure evolution predictions via surrogate models trained by machine learning methods. *npj Comput. Mater.* **7**, 3 (2021).
100. Pandey, A. & Pokharel, R. Machine learning based surrogate modeling approach for mapping crystal deformation in three dimensions. *Scr. Mater.* **193**, 1–5 (2021).

101. Teichert, G. H. & Garikipati, K. Machine learning materials physics: Surrogate optimization and multi-fidelity algorithms predict precipitate morphology in an alternative to phase field dynamics. *Comput. Methods Appl. Mech. Engrg.* **344**, 666–693 (2019).
102. Herman, E., Stewart, J. A. & Dingreville, R. A data-driven surrogate model to rapidly predict microstructure morphology during physical vapor deposition. *Appl. Math. Model.* **88**, 589–603 (2020).
103. Nyshadham, C. et al. Machine-learned multi-system surrogate models for materials prediction. *npj Comput. Mater.* **5**, 51 (2019).
104. Peivaste, I. et al. Machine-learning-based surrogate modeling of microstructure evolution using phase-field. *Comput. Mater. Sci.* **214**, 111750 (2022).
105. Zhang, X. X. & Garikipati, K. Machine learning materials physics: Multi-resolution neural networks learn the free energy and nonlinear elastic response of evolving microstructures. *Comput. Methods Appl. Mech. Engrg.* **372**, 113362 (2020).
106. Kunwar, A., Malla, P. B., Sun, J. H., Qu, L. & Ma, H. T. Convolutional neural network model for synchrotron radiation imaging datasets to automatically detect interfacial microstructure: An in situ process monitoring tool during solar PV ribbon fabrication. *Sol. Energy* **224**, 230–244 (2021).
107. Abram, M., Burghardt, K., Ver Steeg, G., Galstyan, A. & Dingreville, R. Inferring topological transitions in pattern-forming processes with self-supervised learning. *npj Comput. Mater.* **8**, 1 (2022).
108. Hui, X. et al. Growth competition between columnar dendrite and degenerate seaweed during directional solidification of alloys: Insights from multi-phase field simulations. *Mater. Des.* **185**, 108250 (2020).
109. Kiyani, E., Silber, S., Kooshkbaghi, M. & Karttunen, M. Machine-learning-based data-driven discovery of nonlinear phase-field dynamics. *Phys. Rev. E* **106**, 065303 (2022).
110. Tourret, D., Liu, H. & Llorca, J. Phase-field modeling of microstructure evolution: recent applications, perspectives and challenges. *Prog. Mater. Sci.* **123**, 100810 (2021).
111. Vilalta, P. C., Sheikholeslami, S., Ruiz, K. S., Yee, X. C. & Koslowski, M. Machine Learning for Predicting the Critical Yield Stress of High Entropy Alloys. *J. Eng. Mater. -Technol.* **143**, 021005 (2021).
112. Karan, V., Indresh, A. M. & Bhattacharya, S. Accelerated Solutions of Coupled Phase-Field Problems using Generative Adversarial Networks. Preprint at https://arxiv.org/pdf/2211.12084.pdf (2022).
113. Hu, C., Martin, S. & Dingreville, R. Accelerating phase-field predictions via recurrent neural networks learning the microstructure evolution in latent space. *Comput. Methods Appl. Mech. Engrg.* **397**, 115128 (2022).
114. Fetni, S. et al. Capabilities of Auto-encoders and Principal Component Analysis of the reduction of microstructural images; Application on the acceleration of Phase-Field simulations. *Comput. Mater. Sci.* **216**, 111820 (2023).
115. Koeppe, A., Bamer, F., Hernandez Padilla, C. A. & Markert, B. Neural network representation of a phase-field model for brittle fracture. *PAMM-Proc. Appl. Math. Mech.* **17**, 253–254 (2017).
116. Yang, K. Q. et al. Self-supervised learning and prediction of microstructure evolution with convolutional recurrent neural network. *Patterns* **2**, 100243 (2021).
117. Yi Gong, Q., DeWitt, S., Radhakrishnan, B. & Biros, G. GrainNN: A neighbor-aware long short-term memory network for predicting microstructure evolution during polycrystalline grain formation. *Comput. Mater. Sci.* **218**, 111927 (2023).
118. Li, W., Bazant, M. Z. & Zhu, J. Phase-Field DeepONet: Physics-informed deep operator neural network for fast simulations of pattern formation governed by gradient flows of free-energy functionals. Preprint at https://arxiv.org/pdf/2302.13368.pdf (2023).
119. Goswami, S., Yin, M. L., Yu, Y. & Karniadakis, G. E. A physics-informed variational DeepONet for predicting crack path in quasi-brittle materials. *Comput. Method. Appl. M.* **391**, 114587 (2022).
120. Oommen, V., Shukla, K., Goswami, S., Dingreville, R. & Karniadakis, G. E. Learning two-phase microstructure evolution using neural operators and autoencoder architectures. *npj Comput. Mater.* **8**, 190 (2022).
121. Li, Z. Y. et al. Fourier neural operator for parametric partial differential equations. Preprint at https://arxiv.org/pdf/2010.08895 (2020).
122. Wen, G., Zong, Yi,L., Azizzadenesheli, K., Anandkumar, A. & Benson, S. M. U-FNO-An enhanced Fourier neural operator-based deep-learning model for multi-phase flow. *Adv. Water Resour.* **163**, 104180 (2022).
123. Burke, E. K. & Kendall, G. *Search Methodologies—Introductory Tutorials in Optimization and Decision Support Techniques*. (Springer US, 2005).
124. Sugathan, S., Thekkepat, K., Bandyopadhyay, S., Kim, J. & Cha, P.-R. A phase field model combined with a genetic algorithm for polycrystalline hafnium zirconium oxide ferroelectrics. *Nanoscale* **14**, 14997–15009 (2022).
125. Desai, S. & Dingreville, R. Learning time-dependent deposition protocols to design thin films via genetic algorithms. *Mater. Des.* **219**, 110815 (2022).
126. Greenwood, M. et al. Quantitative 3D phase field modelling of solidification using next-generation adaptive mesh refinement. *Comput. Mater. Sci.* **142**, 153–171 (2018).
127. Zhang, A. et al. General hierarchical structure to solve transport phenomena with dissimilar time scales: Application in large-scale three-dimensional thermosolutal phase-field problems. *Phys. Rev. E* **102**, 15 (2020).
128. Zhang, A. et al. Multiphase and multiphysics modeling of dendrite growth and gas porosity evolution during solidification. *Acta Mater.* **214**, 117005 (2021).
129. Zhang, A. et al. Solution to Multiscale and Multiphysics Problems: A Phase-Field Study of Fully Coupled Thermal-Solute-Convection Dendrite Growth. *Adv. Theory Simul.* **4**, 2000251 (2021).
130. Xu, W. Q. et al. A phase field method with adaptive refinement strategy and virtual crack insertion technique. *Eng. Fract. Mech.* **271**, 108669 (2022).
131. Nguyen-Thanh, N., Li, W. D., Huang, J. Z. & Zhou, K. Adaptive higher-order phase -field modeling of anisotropic brittle fracture in 3D polycrystalline materials. *Comput. Methods ApplMech. Engrg.* **372**, 113434 (2020).
132. Peng, F., Liu, H. K., Li, S. & Cui, X. Y. Quadtree-polygonal smoothed finite element method for adaptive brittle fracture problems. *Eng. Anal. Bound. Elem.* **134**, 491–509 (2022).
133. Gupta, A., Krishnan, U. M., Mandal, T. K., Chowdhury, R. & Nguyen, V. P. An adaptive mesh refinement algorithm for phase-field fracture models: Application to brittle, cohesive, and dynamic fracture. *Comput. Method. Appl. M.* **399**, 115347 (2022).
134. Proserpio, D., Ambati, M., De Lorenzis, L. & Kiendl, J. Phase-field simulation of ductile fracture in shell structures. *Comput. Methods Appl Mech. Engrg.* **385**, 114019 (2021).
135. Nguyen, T.-T., Réthoré, J., Yvonnet, J. & Baietto, M.-C. Multi-phase-field modeling of anisotropic crack propagation for polycrystalline materials. *Comput. Mech.* **60**, 289–314 (2017).
136. Guo, Y. Q., Luo, S., Wang, W. L. & Zhu, M. Y. A GPU-accelerated 3D PF-LBM modelling of multi-dendritic growth in an undercooled melt of Fe–C binary alloy. *J. Mater. Res. Technol.* **17**, 2059–2072 (2022).
137. Gao, A. et al. GPU-accelerated phase field simulation of directional solidification. *Sci. China-Technol. Sci.* **57**, 1191–1197 (2014).
138. Yamanaka, A., Aoki, T., Ogawa, S. & Takaki, T. GPU-accelerated phase-field simulation of dendritic solidification in a binary alloy. *J. Cryst. Growth* **318**, 40–45 (2011).
139. Zhu, C. S., Liu, J. Q., Zhu, M. F. & Feng, L. Multi-GPU hybrid programming accelerated three-dimensional phase-field model in binary alloy. *AIP Adv.* **8**, 035312 (2018).
140. Zhu, C. S., Guo, X. T., Feng, L., Idemudia, C. U. & Jin, X. Simulation of three-dimensional eutectic growth multi-phase field based on OpenCL parallel. *AIP Adv.* **10**, 025026 (2020).
141. Zhu, C. S., Deng, Z. Y., Feng, L. & Li, Y. J. Simulation of eutectic growth using phase field method and LBM based on OpenCL. *Comp. Mater. Sci.* **176**, 109523 (2020).
142. Zhu, C. S., Li, Y. J., Ma, F. L., Feng, L. & Lei, P. Three-dimensional multi-phase-field simulation of eutectoid alloy based on OpenCL parallel. *China Foundry* **18**, 239–248 (2021).
143. Tennyson, P. G., Karthik, G. M. & Phanikumar, G. MPI plus OpenCL implementation of a phase-field method incorporating CALPHAD description of Gibbs energies on heterogeneous computing platforms. *Comput. Phys. Commun.* **186**, 48–64 (2015).
144. Gao, Z. H. et al. Multi-phase field model simulation based on MPI+ OpenMP parallel: Evolution of seaweed and dendritic structure in directional solidification. *AIP Adv.* **12**, 035018 (2022).
145. Fromm, B. S., Chang, K., Mcdowell, D. L., Chen, L. Q. & Garmestani, H. Linking phase-field and finite-element modeling for process-structure-property relations of a Ni-base superalloy. *Acta Mater.* **60**, 5984–5999 (2012).
146. Min, K. M. et al. Integrated crystal plasticity and phase field model for prediction of recrystallization texture and anisotropic mechanical properties of cold-rolled ultra-low carbon steels. *Int. J. Plast.* **127**, 102644 (2020).
147. Zhang, J. H. et al. Phase field simulation of the stress-induced α microstructure in Ti-6Al-4 V alloy and its CPFEM properties evaluation. *J. Mater. Sci. Technol.* **90**, 168–182 (2021).
148. Léonard, F. & Desai, R. C. Spinodal decomposition and dislocation lines in thin films and bulk materials. *Phys. Rev. B* **58**, 8277–8288 (1998).
149. Gao, S. W. et al. Primary combination of phase-field and discrete dislocation dynamics methods for investigating athermal plastic deformation in various realistic Ni-base single crystal superalloy microstructures. *Model. Simul. Mat. Sci. Eng.* **23**, 075003 (2015).
150. Gao, S. W., Fivel, M., Ma, A. & Hartmaier, A. Influence of misfit stresses on dislocation glide in single crystal superalloys: A three-dimensional discrete dislocation dynamics study. *J. Mech. Phys. Solids* **76**, 276–290 (2015).
151. Gao, S. W. et al. A phenomenological creep model for Nickel-base single crystal superalloys at intermediate temperatures. *Model. Simul. Mat. Sci. Eng.* **26**, 055001 (2018).
152. Wu, R. H. & Sandfeld, S. Insights from a minimal model of dislocation-assisted rafting in single crystal Nickel-based superalloys. *Scr. Mater.* **123**, 42–45 (2016).

153. Wu, R. H., Yue, Z. F. & Wang, M. Effect of initial gamma/gamma' microstructure on creep of single crystal nickel-based superalloys: A phase-field simulation incorporating dislocation dynamics. *J. Alloy. Compd.* **779**, 326–334 (2019).
154. Wu, R. H. & Zhang, Y. F. Phase-field, dislocation based plasticity and damage coupled model: modelling and application to single crystal superalloys. *Int. J. Plast.* **157**, 103376 (2022).
155. Gaubert, A., Bouar, Y. L. & Finel, A. Coupling phase field and viscoplasticity to study rafting in Ni-based superalloys. *Philos. Mag.* **90**, 375–404 (2010).
156. Harikrishnan, R. & Le Graverend, J.-B. A creep-damage phase-field model: Predicting topological inversion in Ni-based single crystal superalloys. *Mater. Des.* **160**, 405–416 (2018).
157. Yang, M. et al. A phase-field model for creep behavior in nickel-base single-crystal superalloy: Coupled with creep damage. *Scr. Mater.* **147**, 16–20 (2018).
158. Yu, Z. Y., Wang, X. M., Yue, Z. F. & Sun, S. Y. Visco-plasticity phase-field simulation of the mechanical property and rafting behavior in nickel-based superalloys. *Intermetallics* **125**, 106884 (2020).
159. Liu, P. W. et al. Integration of phase-field model and crystal plasticity for the prediction of process-structure-property relation of additively manufactured metallic materials. *Int. J. Plast.* **128**, 102670 (2020).
160. Rahnama, A., Kotadia, H. & Sridhar, S. Effect of Ni alloying on the microstructural evolution and mechanical properties of two duplex light-weight steels during different annealing temperatures: experiment and phase-field simulation. *Acta Mater.* **132**, 627–643 (2017).
161. Cai, Y. *Phase field modeling of microstructure evolution during hot deformation for AZ80 magesium alloy and its application* Doctor thesis, (University of Science and Technology Beijing, 2019).
162. Cai, Y. et al. An isothermal forming process with multi-stage variable speed for magnesium component assisted by sensitivity analysis. *Mater. Sci. Eng. A.* **729**, 9–20 (2018).
163. Cai, Y. et al. Phase field modeling of discontinuous dynamic recrystallization in hot deformation of magnesium alloys. *Int. J. Plast.* **133**, 102773 (2020).
164. Geng, S. N. et al. Effects of back-diffusion on solidification cracking susceptibility of Al-Mg alloys during welding: A phase-field study. *Acta Mater.* **160**, 85–96 (2018).
165. Geng, S. N. et al. Comparison of solidification cracking susceptibility between Al-Mg and Al-Cu alloys during welding: A phase-field study. *Scri. Mater.* **150**, 120–124 (2018).
166. Geng, S. N., Jiang, P., Shao, X. Y., Guo, L. Y. & Gao, X. S. Heat transfer and fluid flow and their effects on the solidification microstructure in full-penetration laser welding of aluminum sheet. *J. Mater. Sci. Technol.* **46**, 50–63 (2020).
167. Geng, S. N. *Multi-scale Simulation of the Mircrostructure Evolution during Solidification in Laser Welding of Aluminum Alloy Sheet*, doctor thesis. (Huazhong University of Science and Technology, 2020).
168. Qiu, C. R. et al. Transparent ferroelectric crystals with ultrahigh piezoelectricity. *Nature* **577**, 350–354 (2020).
169. Cao, J. M., Liu, M. X., Liu, Z. L., Hou, H. & Zhao, Y. H. Alternating Current Field Effects in Atomically Ferroelectric Ultrathin Films. *Materials* **15**, 2506 (2022).
170. Momeni, K. et al. Multiscale computational understanding and growth of 2D materials: a review. *npj Comput. Mater.* **6**, 1–18 (2020).
171. Berry, J. & Grant, M. Phase-field-crystal modeling of glass-forming liquids: Spanning time scales during vitrification, aging, and deformation. *Phys. Rev. E* **89**, 062303 (2014).
172. Li, Y. et al. Effect of grain structure and strain rate on dynamic recrystallization and deformation behavior: A phase field-crystal plasticity model. *Comp. Mater. Sci.* **180**, 109707 (2020).
173. Chen, Y. et al. Exploring the structure-property relationship of three-dimensional hexagonal boron nitride aerogels with gyroid surfaces. *Nanoscale* **12**, 10180–10188 (2020).
174. Moats, K. A., Asadi, E. & Laradji, M. Phase field crystal simulations of the kinetics of Ostwald ripening in two dimensions. *Phys. Rev. E* **99**, 012803 (2019).
175. Lavrskyi, M., Zapolsky, H. & Khachaturyan, A. G. Quasiparticle approach to diffusional atomic scale self-assembly of complex structures: from disorder to complex crystals and double-helix polymers. *npj Comput. Mater.* **2**, 1–9 (2016).
176. Chen, L. Q. Phase-field models for microstructure evolution. *Annu. Rev. Mater. Res.* **32**, 113–140 (2002).
177. Boettinger, W. J., Warren, J. A., Beckermann, C. & Karma, A. Phase-field simulation of solidification. *Annu. Rev. Mater. Res.* **32**, 163–194 (2002).
178. Chen, L. Q. & Zhao, Y. H. From Classical Thermodynamics to Phase-field Method. *Prog. Mater. Sci.* **124**, 100868 (2022).
179. Emmerich, H. Advances of and by phase-field modelling in condensed-matter physics. *Adv. Phys.* **57**, 1–87 (2008).
180. Qin, R. S. & Bhadeshia, H. K. Phase field method. *Mater. Sci. Technol.* **26**, 803–811 (2010).
181. Granasy, L. et al. Phase-field modeling of crystal nucleation in undercooled liquids—A review. *Prog. Mater. Sci.* **106**, 100569 (2019).
182. Cahn, J. W. & Hilliard, J. E. Free Energy of a Nonuniform System. I. Interfacial Free Energy. *J. Chem. Phys.* **28**, 250–258 (1958).
183. Allen, S. M. & Cahn, J. W. Ground state structures in ordered binary alloys with second neighbor interactions. *Acta Mater.* **20**, 423–433 (1972).
184. Zhao, Y. H. Editorial: Phase field method and integrated computing materials engineering. *Front. Mater.* **10**, 1145833 (2023).
185. Wang, S., Xue, C., Yang, X., Tian, G. & Wang, J. Heterogeneous nucleation of T1 precipitates in solid solution of Al-Cu-Li alloys from Ag-rich structures: An ab initio study. *Sci. Mater.* **225**, 115191 (2023).
186. Wei, X.-K. et al. Ferroelectric phase-transition frustration near a tricritical composition point. *Nat. Commun.* **12**, 5322 (2021).
187. Luo, Z., Burrows, S. A., Fan, X., Smoukov, S. K. & Boek, E. S. Virtual voids method to generate low-density microporous carbon structures using quenched molecular dynamics simulation. *Carbon* **183**, 438–448 (2021).
188. Viardin, A., Zaloznik, M., Souhar, Y., Apel, M. & Combeau, H. Mesoscopic modeling of spacing and grain selection in columnar dendritic solidification: Envelope versus phase-field model. *Acta Mater.* **122**, 386–399 (2017).
189. Teferra, K. & Rowenhorst, D. J. Optimizing the cellular automata finite element model for additive manufacturing to simulate large microstructures. *Acta Mater.* **213**, 116930 (2021).
190. Geng, S. N., Ping, J., Guo, L. Y., Gao, X. S. & Mi, G. Y. Multi-scale simulation of grain/sub-grain structure evolution during solidification in laser welding of aluminum alloys. *Int. J. Heat. Mass Tranf.* **149**, 119252 (2019).

ACKNOWLEDGEMENTS

This work was supported by the talent start-up funds of Beijing Advanced Innovation Center for Materials Genome Engineering of University of Science and Technology Beijing, and Professor JX Xie gives valuable guidance on the concept and understanding of "Integrated Computational Materials Engineering". Also supported by National Natural Science Foundation of China (Nos. 52074246, 52201146, 52205429, 52275390), National Defense Basic Scientific Research Program of China (No. JCKY2020408B002) and Key Research and Development Program of Shanxi Province (202102050201011). Many thanks to Dr. XL Tian of North University of China for her kind effort and time in checking, processing, and editing, and Professor L.Q. Chen of Pennsylvania State University for his invitation and critical feedback.

AUTHOR CONTRIBUTIONS

Y.H.Z. conceived the idea and wrote the review.

COMPETING INTERESTS

The author declares no competing interests.

ADDITIONAL INFORMATION

Supplementary information The online version contains supplementary material available at https://doi.org/10.1038/s41524-023-01038-z.

Correspondence and requests for materials should be addressed to Yuhong Zhao.

Reprints and permission information is available at http://www.nature.com/reprints

Publisher's note Springer Nature remains neutral with regard to jurisdictional claims in published maps and institutional affiliations.